Classification of rock slope cavernous weathering on UAV photogrammetric point clouds: The example of Hegra (UNESCO World Heritage Site, Kingdom of Saudi Arabia)

Tommaso Beni [a],[*], Lorenzo Nava [b], Giovanni Gigli [a], William Frodella [a], Filippo Catani [b], Nicola Casagli [a], José Ignacio Gallego [c], Claudio Margottini [d], Daniele Spizzichino [d],[e]

[a] Department of Earth Sciences, University of Florence, Via Giorgio la Pira 4, 50121 Florence, Italy
[b] Machine Intelligence and Slope Stability Laboratory, Department of Geosciences, University of Padova, 35129 Padova, Italy
[c] Kingdoms Institute – Royal Commission for AlUla, AlUla, Saudi Arabia
[d] UNESCO Chair on the Prevention and Sustainable Management of Geo-Hydrological Hazards, University of Florence, Largo Enrico Fermi 2, 50125 Florence, Italy
[e] ISPRA, Department for Geological Survey of Italy, via Vitaliano Brancati 48, 00144 Rome, Italy

ARTICLE INFO

ABSTRACT

The analysis of three-dimensional point cloud data is becoming one of the most used approaches to assess instabilities processes affecting rock slopes. With the increased collection of point cloud data, there is an increasing demand for rapid computational point cloud segmentation techniques to format data for rock fall risk analysis. However, there is a scarcity of semantic segmentation research focusing on geological data and the practical issues they pose. In this study, we propose a novel application to automatically define the spatial extent and intensity of weathered rock slope areas. The studied rock slopes are in Hegra Archaeological Site (al-Hijr / Madā̓ in Ṣāliḥ), the first UNESCO World Heritage area inscribed in the Kingdom of Saudi Arabia (KSA) in 2008. Here, cavernous weathering processes, with honeycombs and *tafoni* features, affect the carved rock slope and increase the rockfall hazard. With the spread and improvement of close-range methods, such as Terrestrial Laser Scanner (TLS) and Unmanned Aerial Vehicle Digital Photogrammetry (UAV-DP), it is possible to obtain fast and accurate high-resolution point cloud data of the studied scenario, i.e., rock mass. This paper presents the automated mapping results obtained by a combination of explainable artificial intelligence (XAI) algorithms and three-dimensional geometric analysis of a point cloud using the geometric feature tools available for free on CloudCompare (CC) open-source software. Three-dimensional data were obtained using the UAV-DP technique. The proposed workflow allows, using random forest modelling (RF), to quantify the cavernous weathering extent and estimate the relative intensity on the rock slope, faster than using traditional time-consuming manual segmentation processes. The RF model was able to accurately forecast the cavernous weathering regions (accuracy of up to 85%), with a slight propensity to underpredict, as indicated by the somewhat low recall ($\sim$ 63%), and a limited number of false positives, as indicated by the high precision (up to 84%). This approach is easily reproducible at low cost in terms of computational, human, and financial resources. The results highlight the reliability of the proposed method for the preliminary assessment of cavernous erosional features with the aim of future assessment, monitoring, and deeper analysis of rock-carved slopes.

1. Introduction

Over the last twenty years, several multidisciplinary non-invasive monitoring techniques and methodologies have been developed to study and classify weathering and deterioration issues affecting cultural heritage, rupestrian settlements, rock-carved monuments, geoparks, and geosites (Boldini et al., 2018; Frodella et al., 2020; Sampietro-Vattuone and Peña-Monné, 2021). Natural and man-made heritage sites are continuously exposed and threatened by natural hazards such as landslides, earthquakes, flooding, and anthropogenic damage (Heinrichs, 2008; Margottini et al., 2016; Paradise, 2013). Rock-carved heritage depends strictly on the materials that constitute the rock slope. Among
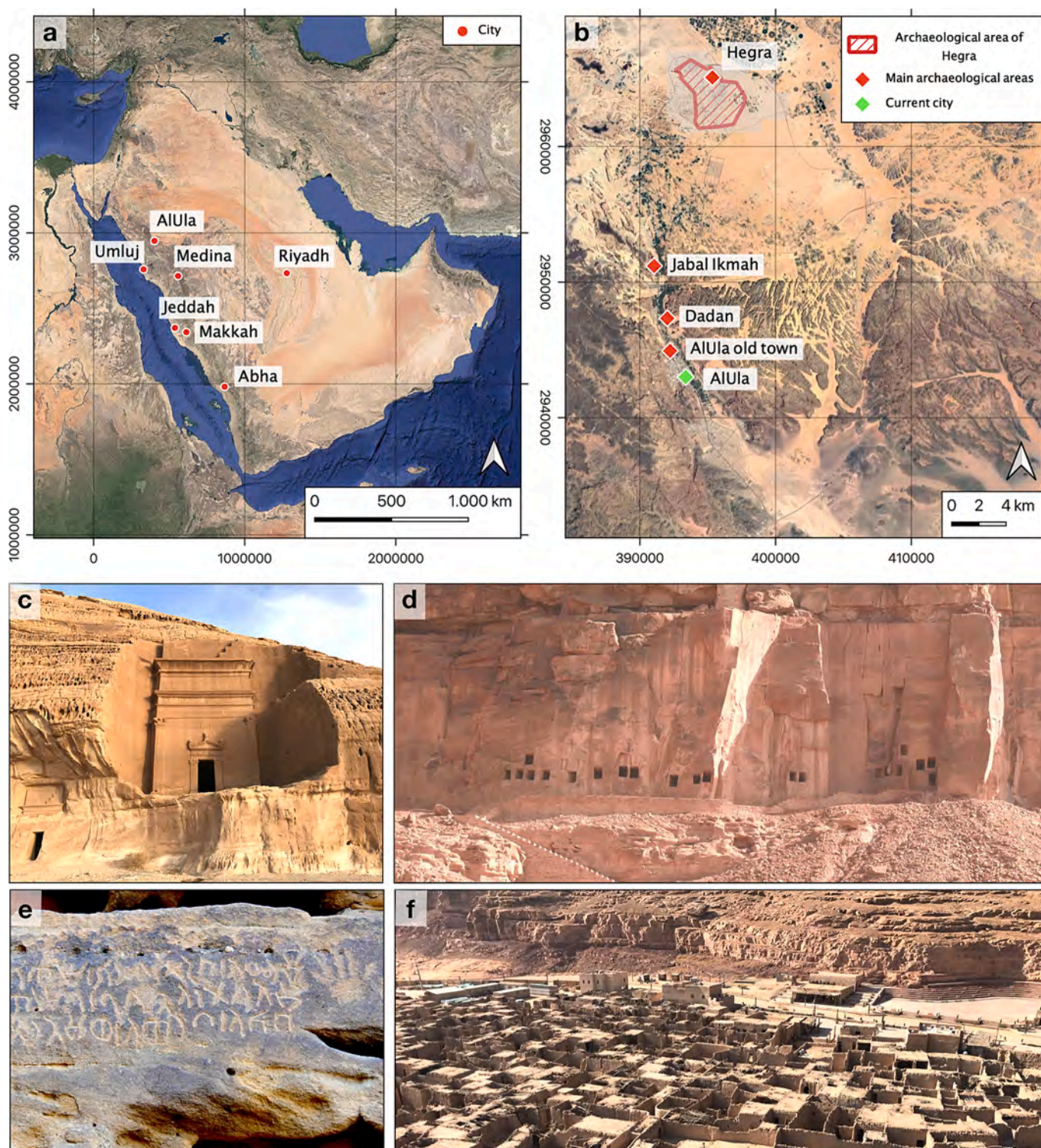
Fig. 1. Geographic location and photos of the main cultural heritage sites of north-western KSA: a) most important projects within the Vision 2030 strategic framework; b) most important archaeological sites in the area of study; in dashed red the study site; c) tomb number 2 in the necropolis of Qasr al-Bint in Hegra, (Nehmé et al., 2015); d) tombs in the ancient city of Dadan, capital of the Dadanite and Lihyanite kingdoms; e) inscriptions at Jabal Ikmah; f) view from above of AlUla Old Town. (For interpretation of the references to colour in this figure legend, the reader is referred to the web version of this article.)

these, sedimentary soft rocks such as sandstones represent a challenge for conservation issues. Several heritage sites that constitute the most remarkable cultural heritage of the Kingdom of Saudi Arabia (KSA) and important examples of landscapes are made of sandstone (Fig. 1).

In 2019, the Saudi Government introduced a tourist visa to develop the tourism industry, with clear beacons. Since then, there has been a continuous increase in the number of tourists coming from outside the Kingdom. Following the Vision 2030 strategic framework and the National Tourism Strategy's milestones, the main goal of the KSA is to attract 100 million annual visits in 2030 (Vision, 2022). Therefore, the protection and conservation of cultural heritage are becoming one of the main pressing issues in the KSA, not only from the archaeological and safety point of view but also for society, in terms of local and national economies. Tourism is playing a key role in the expected evolution of the Kingdom, in present and future years (Vision, 2022).

Currently, close-range methods such as Terrestrial Laser Scanner (TLS) and Unmanned Aerial Vehicle Digital Photogrammetry (UAV-DP) are one of the most used techniques in the field of rock-carved cultural heritage to assess and monitor potential failures affecting the rock mass and to evaluate global slope stability. These approaches allow the acquisition of high-density three-dimensional point clouds of the studied targets. TLS and UAV-DP-derived data have been increasingly employed for rockfall hazard assessment (Beni et al., 2022; Menegoni et al., 2019), discontinuity mapping (Battulwar et al., 2021; Gigli and Casagli, 2011), geomorphological studies (Sturzenegger and Stead, 2009; Weidner et al., 2021), slope stability analysis and landslide monitoring (Balek and Blahůt, 2017; Pellicani et al., 2019). In addition, repeated scanning can be used for centimetric-to-millimetric displacement evaluations (Abellán et al., 2009). Raw point clouds are the starting point for simple task analysis, such as visualization, and for deeper analysis, such as computing geometric features (Hackel et al., 2016; Weinmann et al., 2013, 2017), scalar fields interpolation, multiscale model-to-model comparison and cloud to cloud distances calculation (DiFrancesco et al., 2020; Lague et al., 2013). Currently, several free and open-source software and algorithms enable us to create, view and manage three-dimensional data and to carry out 3D point cloud analysis (Liu et al., 2021). Many authors have demonstrated the potential of the open-source CloudCompare (CC) processing software (CloudCompare, 2022) for processing point cloud data for earth science issues (Blomley et al., 2014; Froideval et al., 2019; Hackel et al., 2016; Mao et al., 2021) and to perform binary classification of point clouds (Brodu and Lague, 2012). However, the optimization of automated methods to support the manual labelling of point clouds is still a research field of growing interest. One of the main goals when working on point cloud data is to classify the points on your needs. An example from this study is the manual identification of weathered areas on rock slopes, which is a nontrivial and time-consuming task that is subject to the experience of the operator. It is feasible for a local dataset, but it becomes complicated for an extended three-dimensional dataset, i.e., hundreds of m^2 and tens of millions of points. To address this issue, basic point cloud interpretation tasks like classification (also known as semantic segmentation), have recently been achieved using computer vision methods (Xie et al., 2020). These algorithms are typically created for urban applications and, therefore, do not consider the complexities inherent to geological data (Blomley et al., 2014; Nava et al., 2022; Weinmann et al., 2017). In particular, there are considerations for model design, feature extraction, and validation because the object types that are important to geology and engineering applications frequently differ from urban applications. The development of sophisticated representation learning models, such as PointCNN (Li et al., 2018), which automatically extract features directly from the unorganized points, represents the present state of the art in research on computer vision now. However, the black-box characteristics of the attributes, requirement of large, annotated datasets and computing resource constraints currently limit the application of these techniques. Consequently, research on conventional machine learning techniques is ongoing for a range of purposes (Becker et al., 2018; Pirotti

and Tonion, 2019). However, for geoscience challenges, there are no standard algorithms or extended reference point cloud databases like there are for more general picture classification tasks. Nowadays, several ML-based approaches to automate the semantic segmentation of point clouds in the geologic field have been proposed, see Blanco et al. (2022), Zoumpekas et al. (2021) and references therein, in particular by Weidner et al. (2019, 2021). Concerning the latter, in Weidner et al., 2019, geometric, difference, and intensity features are used in combination with Random Forest (RF), to define four classes: snow, talus, rock and vegetation. In Weidner et al., 2021, RF and combinations of geometric, slope, absolute colour, and texture features are used to define five geologically relevant classes: snow, talus, rock, vegetation, and soil. In the past, two main machine learning (ML) approaches have been used to achieve point cloud classification: Support Vector Machines (SVM) and RF (Lin et al., 2014; Weidner et al., 2019). Several works agree that RF is the most performing multi-class classifier algorithm (Breiman, 2001; Pal, 2005). Despite this, in the existing literature, there are few studies dealing with the automatic assessment of weathered rock slopes, even though cavernous weathering is one of the most widespread phenomena in the world (Bruthans et al., 2018; Paradise, 2013). It develops throughout several lithologies and affects coastal areas, hot and cold deserts and historical buildings (Rodriguez-Navarro et al., 1999).

Among the tools available for free on the CC software, the CANUPO suite developed by Brodu and Lague (2012) could be potentially used to deal with similar classification tasks, i.e., binary classification of weathered/non-weathered areas. CANUPO allows to carry out multi-scale geometric features to achieve binary classification for point cloud segmentation and it works well also for detecting erosional surface features. Despite this, Weidner et al. (2021) confirmed that ML approaches can reach higher accuracy than the CANUPO classifier for point cloud segmentation tasks. Furthermore, the CANUPO tool does not return detailed insights about the used multi-scale geometric features (variables) we were interested in analysing. For example, in terms of their SHapley Additive exPlanations (SHAP) values. The latter is a technique employed in machine learning and data analysis to provide insights into the contribution of individual input features towards the predictions made by a model. It enables us to assess the importance of each feature in influencing the final output of the model. By using SHAP, we can gain a better understanding of the relative significance of different features in shaping the model's predictions. Indeed, CANUPO only returns the balanced accuracy and Fisher Discriminant Ratio values to quantify the performance of the classifier.

To achieve the automatic weathering assessment, a detailed analysis of 16 multi-scale geometric features (160 overall variables) was conducted on the available point clouds dataset. Using so many variables in the RF model allowed us to capture complex relationships that may have non-linear boundary features (Weidner et al., 2019) in the classification process. Our proposal could be seen as an improvement of existing algorithms and methods to characterize the point cloud data in terms of cavernous-weathered areas. The study site is the UNESCO World Heritage Site of Hegra (Kingdom of Saudi Arabia) where >130 rock-carved tombs are present (Fig. 1b-c). To highlight the importance of the automatic cavernous weathering assessment, a global kinematic analysis was conducted to define the overall rockfall susceptibility and understand the correlation between instability mechanisms and the weathered surfaces of the rock slopes.

2. Case study: the archaeological site of Hegra

To evaluate the proposed method, the World Heritage Site of Hegra was chosen within the AlUla Governorate (Fig. 1a-c). Hegra was the first UNESCO World Heritage property inscribed by the Kingdom in 2008 ("UNESCO,", 2022). The archaeological area hosts >110 monumental tombs with ornated and elaborated facades carved in sandstone (Bouchaud et al., 2015; Nehmé et al., 2015). Hundreds of tourists visit them every day. Here, peculiar cavernous weathering features, i.e., *tafoni*,
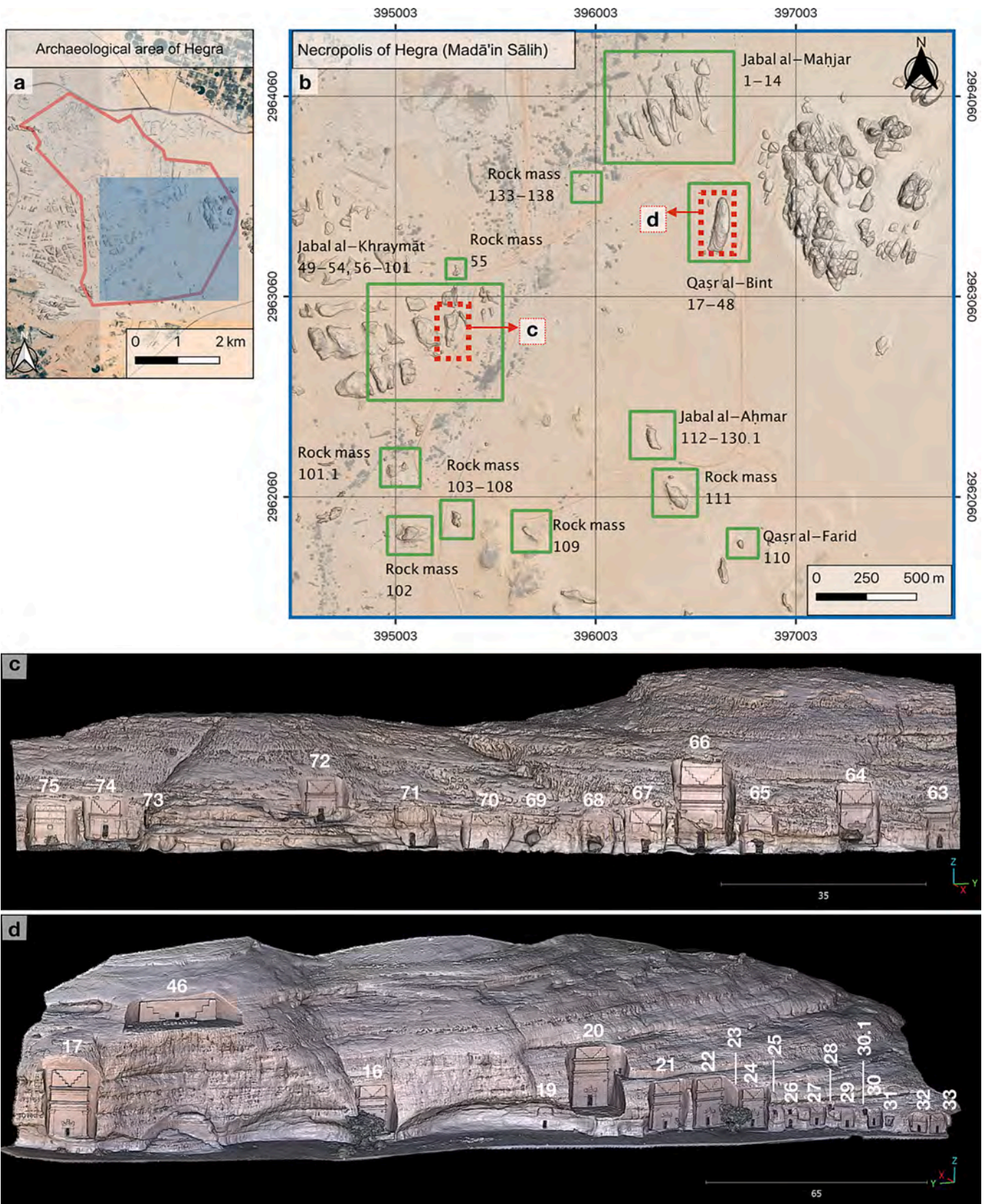
Fig. 2. Location of different items within the Archaeological site of Hegra: a) perimeter of the Archaeological area; b) all the rock masses with the numbers of carved tombs, the two red dotted squares highlight the studied rock slopes: sector II of the Necropolis of Jabal al-Khraymāt (c; site 1) and the Necropolis of Qaṣr al-Bint (d; site 2). In c) and d), the three-dimensional models created by the UAV-DP technique with tombs numbered according to Nehmé et al. (2015). (For interpretation of the references to colour in this figure legend, the reader is referred to the web version of this article.)

alveoli, and honeycomb patterns, affect the rock-carved cultural heritage. Worldwide, the geological and geotechnical characteristics of sandstones *sensu latu* are particularly sensitive to weathering and deterioration processes such as cavernous weathering (Groom et al., 2015; Heinrichs, 2008; Paradise, 2013). These features represent an issue in terms of the conservation and safety of archaeological areas. The presence of cavernous weathering could increase the rockfall slope susceptibility, exposing tourists and tombs to possible damage. In addition, the facades of the tombs carved 2000 years ago (Gallego et al., 2022; Heinrichs, 2008) have also been damaged by the most common weathering phenomena, such as the loss of stone material, alteration, exfoliation, and fissures.

Remarkable rock-carved monuments and heritage sites are located near the city of AlUla (Fig. 1b-f); Hegra, Dadan, AlUla Old Town, and Jabal Ikmah.

To develop and implement the proposed method, we have analysed two rock-slope outcrops in Hegra. One is the sector II of the Necropolis of Jabal al-Khraymāt (site 1; Fig. 2c), and the other is the west side of the Necropolis of Qaṣr al-Bint (site 2; Fig. 2d).

According to Nehmé et al. (Nehmé et al., 2015; Sartre, 2016), the sector II of Jabal al-Khraymāt is characterized by the presence of >15 tombs. This sector represents one of the most endangered of the whole archaeological area. The rock mass is characterized by advanced cavernous weathering and several instability processes.

Furthermore, several tombs are severely damaged (see section 2.2): facades and interiors are not safely accessible to visitors because of possible rock falls and interior roof collapse. Instead, the rock slope of Qaṣr al-Bint is characterized by a lower grade of cavernous weathering (Fig. 2d) with respect to the Jabal al-Khraymāt. It was chosen for this study because it is considered one of the most representative of the whole archaeological area of Hegra, with majestic and well-preserved tombs. Every day, hundreds of tourists visit the necropolis of Qaṣr al-Bint, so there is a higher risk related to potential geo-hazards.

2.1. Geological setting

The geological setting and local climate have played an important role in the evolution of local geomorphology through active weathering processes on rock-carved cultural heritage sites. Primarily, the AlUla and Hegra areas are composed of a Cambro-Ordovician clastic succession (Fig. 3a-b).

These sedimentary rocks are subdivided into three similar formations: Siq Sandstone (Early Cambrian), Quweira Sandstone (Middle-Late Cambrian), and Saq Sandstone (Early Ordovician) (Whabi, 2014). This study focuses on the Quweira Sandstone, which is a massive cross-bedded sandstone, locally silty with common conglomerate zones of quartz and feldspar ("BRGM,", 2022; Donald and Hadly, 1987).

The Archaeological area of Hegra is mainly composed of the middle part of the Quweira Sandstone, which conformably overlies the Upper Siq Sandstone. The middle Quweira sandstone is a succession of fluvial deposits with well-rounded quartz pebbles ranging from millimetres to centimetres (Fig. 3c-e). The cross-bedded sandstone and fining-upward sequences indicate a high-energy fluvial depositional setting. Locally, there are also deformed beds and bioturbation features (Whabi, 2014).

2.2. Cavernous weathering

Cavernous weathering (CW) is one of the most widespread weathering global phenomena (Bruthans et al., 2018; Klimchouk, 2018; Paradise, 2013) developing everywhere in several lithologies and affecting coastal areas, hot and cold deserts, and historical buildings (Rodriguez-Navarro et al., 1999). The morphological term of the cavernous weathering process (or cavernous rock decay features) describes several alteration features and erosional patterns, ranging from millimetres to several meters. The most commonly used terms to describe the forms of this type of weathering are *tafoni*, *alveoli*, and *honeycomb* (Rodriguez-Navarro et al., 1999). Many authors have attempted to propose correct and universal terminology, but there are
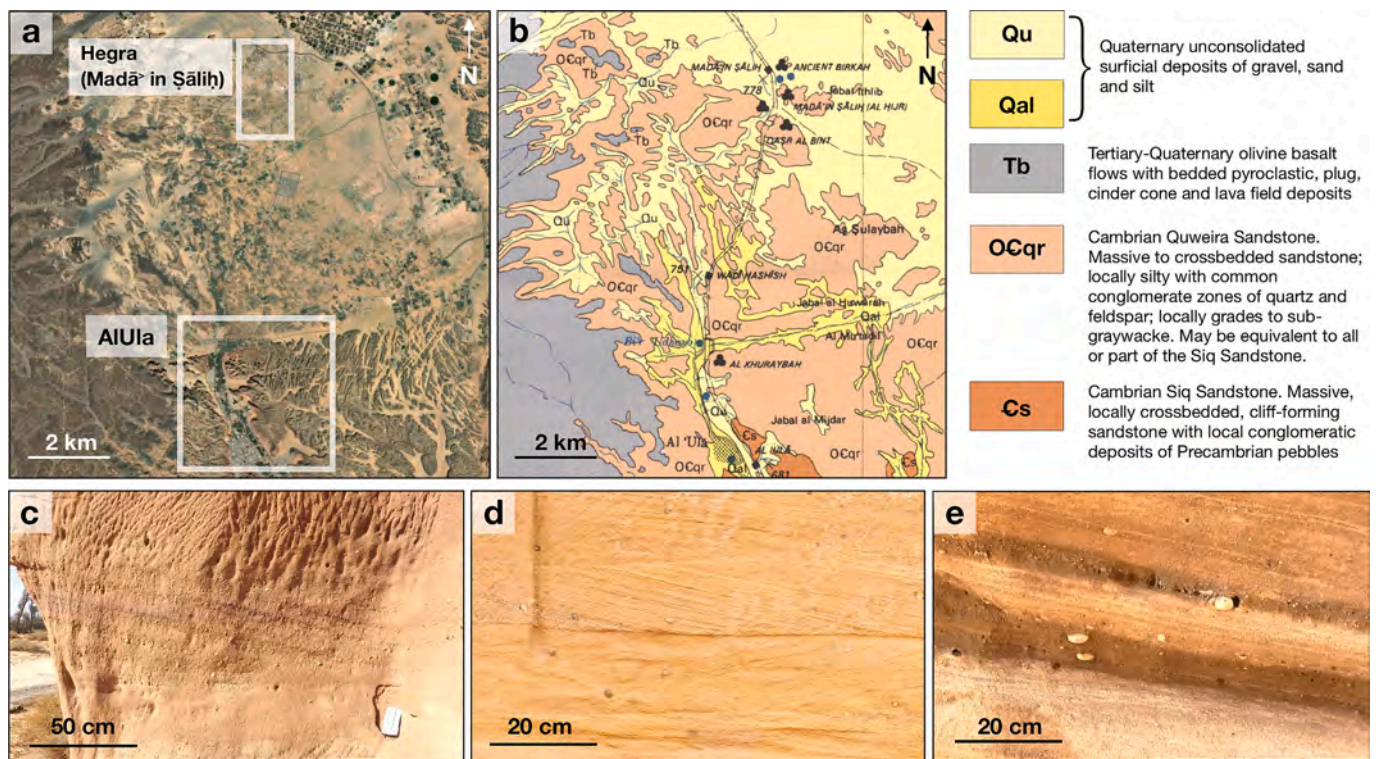

Fig. 3. Geological map of the study area: a) geographic location of the AlUla and Hegra areas; b) geological map of the AlUla area ("BRGM,", 2022) modified after Donald and Hadly (1987); c) massive to cross-bedded sandstone in the Quweira Sandstone at the Necropolis of Jabal al-Maḥjar; d) cross-bedding in the Quweira Sandstone at the Necropolis of Jabal al-Khraymāt; e) particular of the bedding with rounded quartz pebbles in Jabal Ithlib.
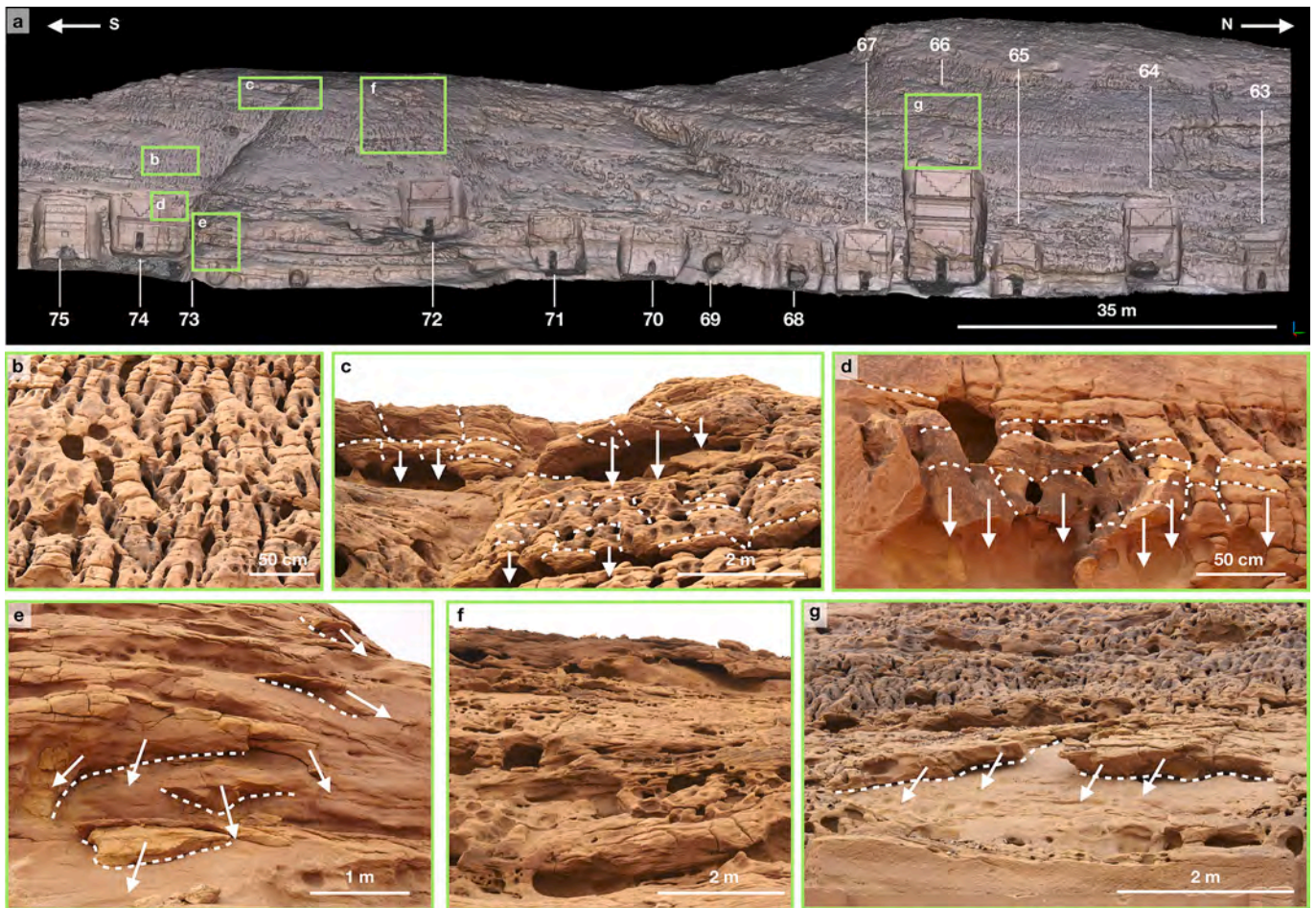
Fig. 4. The investigated slope in the sector II of the Necropolis of Jabal al-Khraymāt in Hegra: a) UAV-DP-obtained three-dimensional model, the green squares highlight some areas affected by both the cavernous weathering features and instability mechanisms; b) particular of the honeycomb pattern; c) *tafoni* and alveoli features that could potentially induce free fall (FF) instability mechanisms; d) *tafoni* and alveoli features causing FF of sandstone blocks; e) area with several blocks prone to plane failure (PF) and FF; f) example of a highly cavernous-weathered rock slope surface; g) alveoli features inducing PF. (For interpretation of the references to colour in this figure legend, the reader is referred to the web version of this article.)

still ambiguities (Groom et al., 2015). In this study we refer to the terminology suggested by Robinson and Williams (1994); *tafoni* (singular *tafone*) for features decimetre- to meter-scale large, alveoli for individual feature centimetre- to decimetre-scale and honeycombs for groups of features (with a pattern) centimetre- to decimetre-scale. In the past, referring to the work of Jennings (1968), *tafoni* features were defined as "forms of cavernous weathering, chiefly found in medium- and coarse-grained, acid to intermediate, crystalline rocks, but also occurring in other rocks such as sandstone, limestone, and schist. These hollows range in diameter and depth from a decimetre or so to several meters, though those smaller than a football are sometimes distinguished as miniature *tafoni*. In shape, they tend to be ellipsoidal or spherical, enlarging inside the opening [...]".

Hollows, both for *tafoni* and honeycomb structures, are often coalescent and separated by thin rock walls and ribs (Klimchouk, 2018). Several authors have tried to understand what are the genetic processes that cause the formation of *tafoni* and alveoli; despite the efforts, it is still an enigmatic and controversial research field (Klimchouk, 2018; Paradise, 2013; Rodriguez-Navarro et al., 1999). Many proposed mechanisms acting individually or together could lead to these erosional features, including salt weathering, wind erosion, thermal changes, variations in clay content in rocks, and a matrix-to-clast ratio (Bruthans et al., 2018; Paradise, 2005). Among them, the combined action of salts and wind seems to play a key role in this weathering process (Rodriguez-Navarro et al., 1999).

In this study, we do not focus on the formation processes that lead to CW features but on their presence, extent, and intensity assessment on the studied rock slopes. *Tafoni* and honeycombs affect the Cambrian rock masses surfaces of Hegra, in which multiple tombs were carved (Figs. 2 and 4), similar to the Paleozoic sandstone of the archaeological site of Petra in Jordan (Heinrichs, 2008; Paradise, 2005, 2013). The action of these features on vertical and sub-vertical rock slopes accelerates sandstone surface recession, worsening the mechanical properties of the rock mass surface and leading to a higher rockfall susceptibility. Several documented instability mechanisms, such as free fall (FF) and plane failure (PF), are induced and facilitated by the action of CW features (Fig. 4c-d-e-g) as confirmed by field surveys. Therefore, the goal of the proposed ML approach is to automatically quantify and localize the extent and intensity of the CW.

3. Materials and methods

The used workflow is shown in Fig. 5.

3.1. UAV-DP point cloud generation

To apply the proposed method, two UAV-DP-generated dense point clouds were used; one is relative to sector II of the Necropolis of Jabal al-Khraymāt and the other to the Necropolis of Qaṣr al-Bint in Hegra. Several acquisition campaigns using UAV have been conducted by the
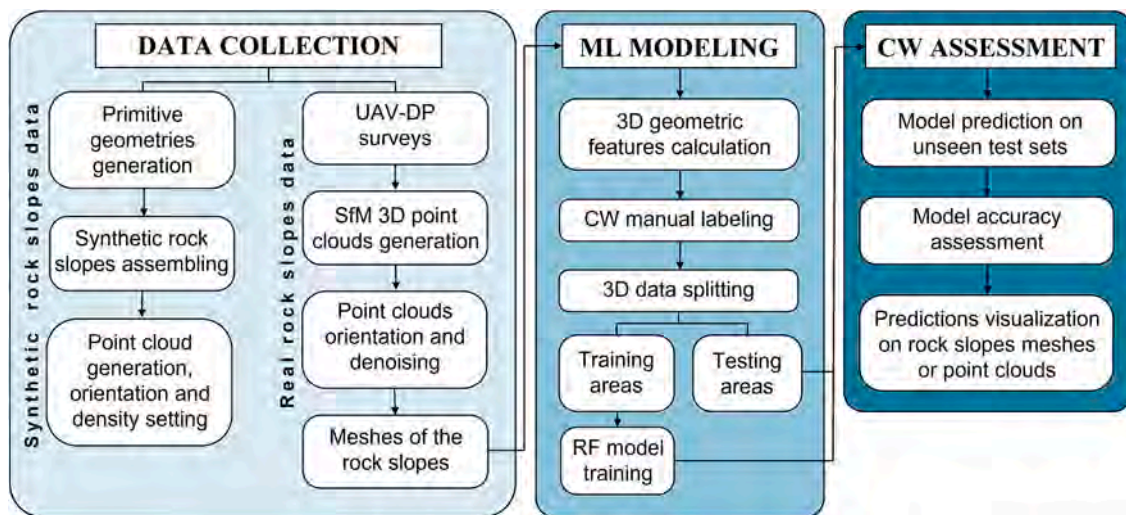
Fig. 5. Flowchart of the proposed method.

Table 1
Technical features of DJI Inspire 2 UAV camera and lens.

Camera Lens	Sensor (mm)	Max aperture (mm)	Image dimensions (rate | pixels)	Resolution (dpi)	Focal length (mm)
ZENMUSE X7 DL 24 mm f/2.8 LSASPH	23.5 × 15.7	f/2.8	3:2 | 6016 × 4008	72	24

Factum Foundation for the Kingdoms Institute of the Royal Commission for AlUla (RCU) as a basic tool for digital conservation and research. >400 images obtained using the UAV-DP technique have been elaborated using a Structure from Motion (SfM) processing software (Pix4D, 2022). Close-range aerial acquisitions were performed using a DJI Inspire 2 quadcopter equipped with a ZENMUSE X7 camera and a DL 24 mm f/2.8 LSASPH lens (Table 1 for technical features).

The flights were carried out using manual trajectories and an image overlap higher than 80% was achieved. To achieve a realistic reconstruction of the rock slope surface, the operators took care to acquire photos under optimal lighting conditions and from several view angles. To prevent any potential inaccuracies in the three-dimensional reconstruction of the inside of the hollows (particularly the "vault" and the "back"), the exposure of each photograph was accurately checked. Consequently, the photogrammetric reconstruction of the interior surfaces of the tafoni and alveoli was facilitated. After the SfM process, a dense point cloud of about 40 million points of the necropolis, with an average ground sample distance (GSD) of approximately 1–2 cm, was created. No Ground Control Points (GCPs) were available. So, manual orientation and scaling were carried out using CC software, aligning the point cloud of the necropolis with respect to the available local digital terrain model (DTM) with a precision of about 1 m using the following tools: translate/rotate tool to roughly align the point cloud with the DTM and then using the iterative closest point (ICP) aligning plug-in. This procedure allowed us to correctly place the point cloud of the necropolis in a three-dimensional space (see Figs. 2c-d and 5a). Decimetric accuracy owing to the internal camera features and overall metric precision in the georeferenced model was achieved. These values are considered acceptable due to the extent of the analysed rock slope and the aim of this study. Also, the potential shifts of the studied UAV-DP clouds along the x, y and z directions, due to the orientation with respect to the available DTM do not affect the point cloud geometric analysis. In fact, the calculated geometric features remain the same even if the model is not georeferenced. The orientation process we achieve was sufficient to orient the cloud with respect to the north direction and the vertical axis with the aim of carrying out the kinematic analysis on the rock slope.

3.2. Geometric features extraction

From the definition proposed by Jennings (1968) about *tafoni* features we know that this kind of erosional hollows "[…] tend to be ellipsoidal or spherical, enlarging inside the opening […]". This was the starting point for the development of this study. In fact, we found out that the analysis of cavernous-weathered surfaces can be solved as a geometric problem analysis of three-dimensional data where the CW features could be approximated as half spheres. Following this idea, a detailed three-dimensional geometrical analysis was carried out using CloudCompare open-source software (CC) on the following point cloud dataset: 1) created ad hoc synthetic rock slopes (Fig. 6a-f); 2) a representative subsample of the UAV-DP-obtained real rock slope point cloud of Jabal al-Khraymāt (Fig. 6g); 3) the whole UAV-DP-obtained real rock slope point clouds (Fig. 2c-d). Datasets 1) and 2) were used to understand how the geometric features work for our issue and dataset 3) was used to apply the ML-aided analysis using the random forest (RF) learning technique.

CC (CloudCompare, 2022) provides tools and plugins to (i) cut and clean point clouds (DiFrancesco et al., 2020), (ii) orient and merge three-dimensional data acquired by different remote sensing (RS) methods (Mao et al., 2021; Son et al., 2020), (iii) compute surface and volume (Son et al., 2020), (iv) apply the iterative closest point (ICP) best-fit algorithm (Kromer et al., 2017), (v) apply the multiscale model-to-model cloud comparison (M3C2) algorithm (Lague et al., 2013) and (vi) calculate displacement and error analysis with cloud-to-cloud distance (C2C) and cloud-to-mesh distance (C2M) plugins. Furthermore, calculate roughness, curvature and other geometric features (Blomley et al., 2014; Hackel et al., 2016; Weidner et al., 2021; Weinmann et al., 2017).

Owing to the complexity of natural outdoor rock-weathered surfaces (see Fig. 6g) the idea of the proposed method lies in exploiting the open-source algorithms proposed by Hackel et al. (2016) and Weinmann et al. (2013), available on CC (CloudCompare, 2022) to compute several geometric features on the studied point cloud to understand, and then using ML-based analysis for our issues.

All the 160 calculated geometric features were treated as variables in the random forest (RF) modelling. For similar tasks, RGB values can also
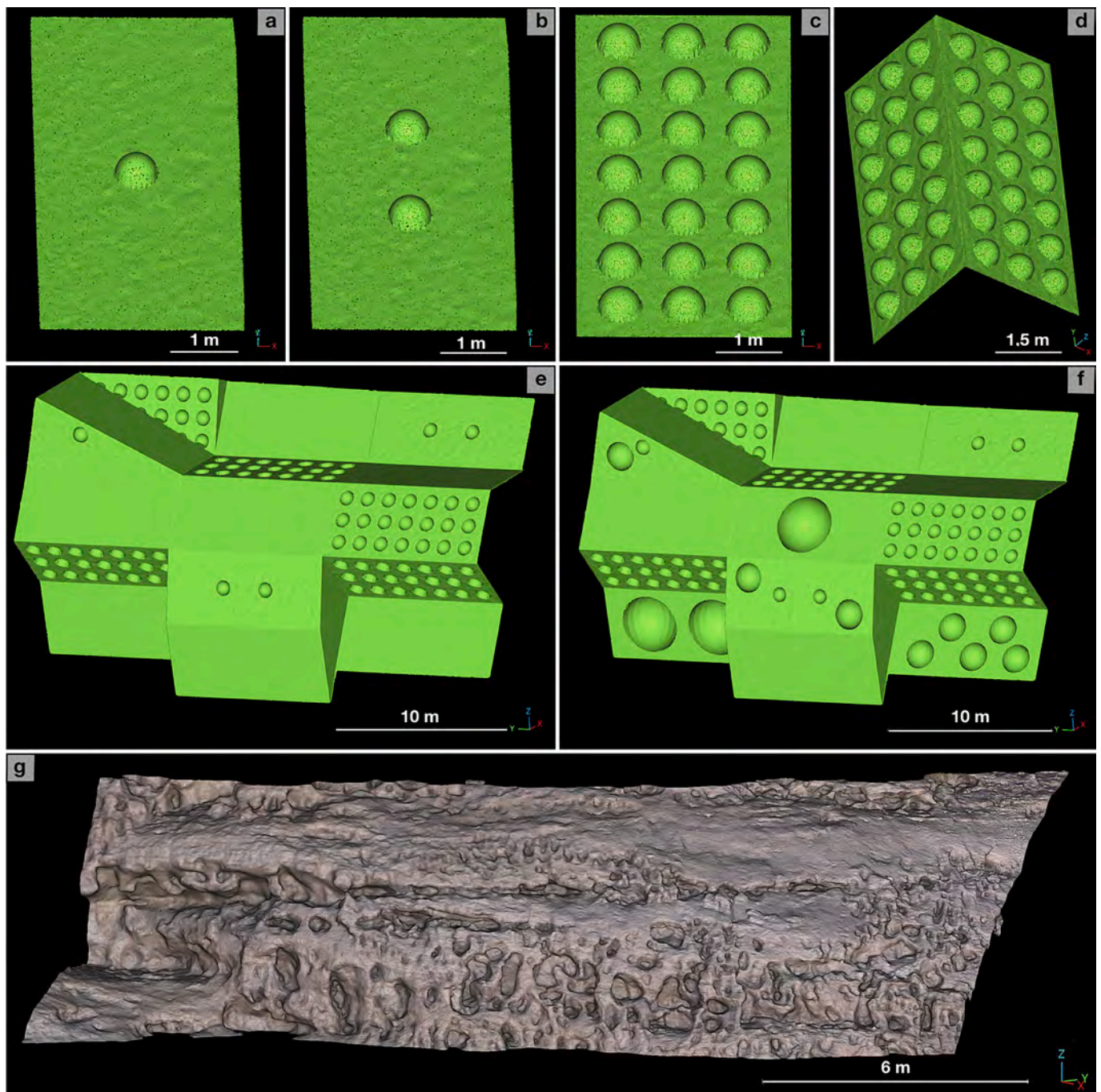
Fig. 6. The three-dimensional synthetic and real dataset used to test all the geometric features with varying kernel radius on cavernous-weathered surfaces: a) one half sphere of 50 cm radius on a flat plane, b) two half spheres, c) twenty-one half spheres, each centre is 1.5 m from the other, and d) forty-two half spheres on two orthogonal flat planes to understand how geometric features work on the edges; e) synthetic cavernous-weathered rock slope with vertical, horizontal and overhanging slopes, all the half spheres have 50 cm radius; f) is the same of e) with the addition of some half spheres of 50 cm, 1 m, and 2 m radius to make a more heterogeneous environment; g) a subsample mesh (and point cloud) of the real weathered rock slope in the sector II of the Necropolis of Jabal al-Khraymāt in Hegra.

be helpful in the classification process for both the UAV-DP and TLS datasets (when RGB values are available; Lichti (2005)). However, for extended three-dimensional rock slopes, the RGB efficiency is biased by the instruments used, moisture surfaces, shadow projections, image exposure variations, etc. To overcome these potential problems, we have decided to use only geometric features to characterize the three-dimensional scenario. Hackel et al. (2016) and Weinmann et al. (2013) have proposed several methods for automatically analyse large three-dimensional point cloud data through semantic interpretation using geometric features. The latter use the eigenvalues ($\lambda_1 \geq \lambda_2 \geq \lambda_3$) of

the eigenvectors (e_1, e_2, e_3) obtained from the covariance matrix calculated in a local neighbourhood of each point (kernel radius) constituting the point cloud. Nowadays, most of the approaches to computing three-dimensional geometric features use data obtained from the local covariance matrix that represents second-order invariant moments within the point positions (Blomley et al., 2014). The geometric features are calculated for each point with respect to the other points falling in a searching sphere with a user-defined radius, i.e., kernel radius. The extraction of the geometric features was carried out for all the available datasets starting from the ones shown in Fig. 6, to
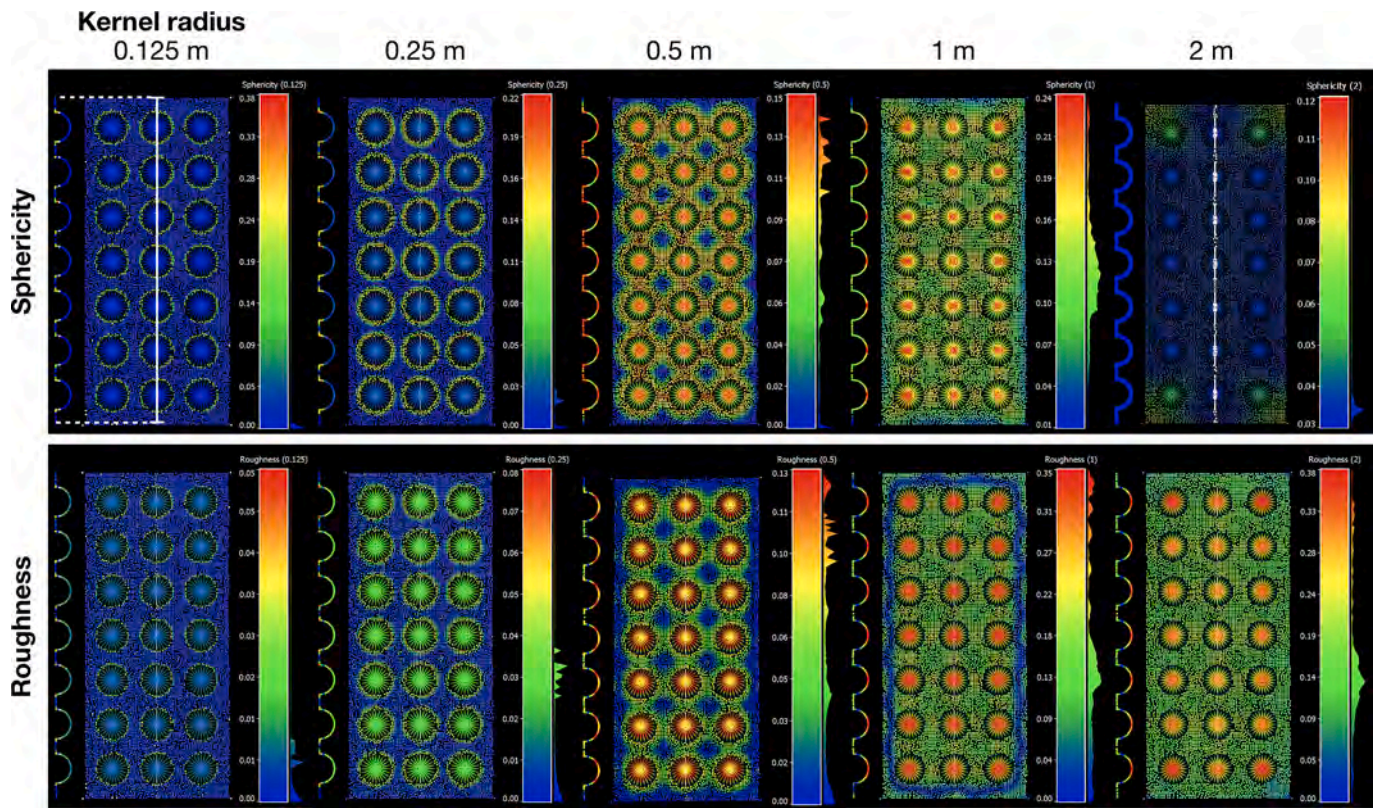
Fig. 7. Example of some geometric features calculated on a synthetic cavernous-weathered point cloud plane (see Fig. 6c), each sphere has a 1 m diameter and the centre-centre distance is 1.5 m from the nearest spheres: a) visualization for some sphericity *S* and roughness *R* values related to different kernel radius (0.125 m, 0.25 m, 0.5 m, 1 m, 2 m); a section (white trace), on the left of each plane, shows how the geometric features work respect to the alveoli shape.

understand how geometric features work, up to the real case scenarios (Fig. 2c-d).

In 2022, the geometric features available on CC are: 1st eigenvalue (λ_1), 2nd eigenvalue (λ_2), 3rd eigenvalue (λ_3) the sum of eigenvalues (Σ) (1), the omnivariance (*O*) (2), the eigenentropy (*E*) (3), the anisotropy (*A*) (4), the planarity (*P*) (5), the linearity (*L*) (6), the sphericity (*S*) (7), PCA1 (8), PCA2 (9), surface variation (*SV*) (10), verticality (*V*) (11) (CloudCompare, 2022; Weinmann et al., 2013).

Follow the definitions:

$$\Sigma = \lambda_1 + \lambda_2 + \lambda_3 \tag{1}$$

$$O = \sqrt[3]{\lambda_1 \cdot \lambda_2 \cdot \lambda_3} \tag{2}$$

$$E = -\sum_{i=1}^{3} \lambda_i \cdot ln(\lambda_i) \tag{3}$$

$$A = \frac{\lambda_1 - \lambda_3}{\lambda_1} \tag{4}$$

$$P = \frac{\lambda_2 - \lambda_3}{\lambda_1} \tag{5}$$

$$L = \frac{\lambda_1 - \lambda_2}{\lambda_1} \tag{6}$$

$$S = \frac{\lambda_3}{\lambda_1} \tag{7}$$

$$PCA1 = \frac{\lambda_1}{\lambda_1 + \lambda_2 + \lambda_3} \tag{8}$$

$$PCA2 = \frac{\lambda_2}{\lambda_1 + \lambda_2 + \lambda_3} \tag{9}$$

$$SV = \frac{\lambda_3}{\lambda_1 + \lambda_2 + \lambda_3} \tag{10}$$

$$V = 1 - n_z \tag{11}$$

where n_z is the third component of the normal vector *n*.

Furthermore, other features are available on CC: roughness *R*, mean curvature C_{mean} and point density. *R* is defined as the shortest distance from a point with respect to the best fitting plane of the other points falling within the searching sphere (a kernel radius of 0.2 m is a searching sphere with a diameter of 0.4 m). The value of C_{mean} depends on the quadric that best fits the points within the kernel radius (CloudCompare, 2022; Har'el, 1995).

There is a close correlation between the kernel radius used and the calculated geometric features on the point cloud dataset (see this dependency in Figs. 7 and 8). So, the dimensionality of the studied target, i. e., hollow dimensions, must be considered as a starting reference to define the multi-scale dimension of the kernel radius and vice-versa.

Moreover, also the density of the point cloud influences the output of the calculated geometric features (Seo, 2021). For these reasons, and for the machine-time elaborations, we always used the same 0.02 m point-to-point distance within the studied synthetic rock slopes (Fig. 6a-f) and the natural ones (Fig. 2c-d and Fig. 6g).

For this study, we have pointed out that there is no literature showing how these algorithms work for the detection of CW features on rock slopes. The principal aims of our study were as follows: i) to devise an automated mapping capable of discerning and delineating the regions on the examined rock slopes that are most affected by cavernous weathering; ii) to obtain quantitative data that can be utilized to conduct further in-depth analyses for the purpose of evaluating rock fall hazards and formulating effective mitigation strategies. To understand the reliability of each geometric feature, several elaborations were carried out
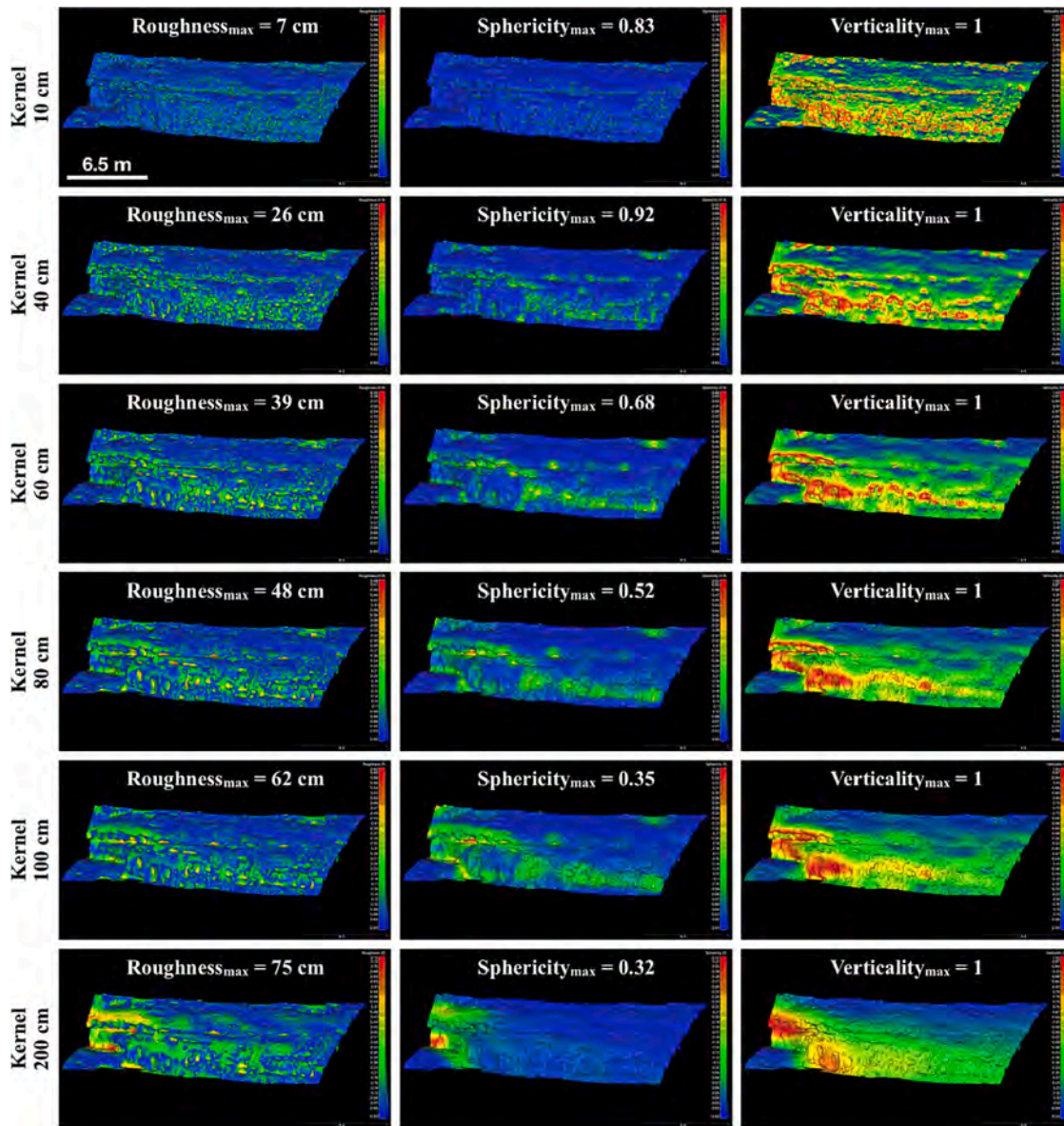
Fig. 8. Example of some geometric features calculated on a real cavernous-weathered rock slope UAV-DP-obtained point cloud (see RGB of this rock slope in Fig. 6g). For each kernel radius value (10 cm, 40 cm, 60 cm, 80 cm, 100 cm, 200 cm) the maximum values reached by *R*, *S,* and *V* are reported. It is well observed how the kernel radius dimensions affect alveoli or *tafoni* identification; the larger the kernel value, the greater the size of the alveoli or *tafoni* identified. For a kernel of 200 cm, the visualization of *S* suggests the presence of *tafoni* (features decimetre- to meter-scale large), for the kernel of 80–100 cm the presence of alveoli (features centimetre- to decimetre-scale).

on the synthetic and real rock slopes using a varying range of the kernel radius, i.e., from 20 to 200 cm with 20 cm steps (Figs. 7 and 8). The proposed workflow can be seen as a multi-scale dimensionality analysis approach based on the hints of the CANUPO classification suite (Brodu and Lague, 2012) together with RF application to point cloud classification, adapted for a complex task such as cavernous-weathered surfaces assessment as a support tool for cultural heritage hazard assessment.

3.3. Random forest (RF)

This ensemble learning technique (Breiman, 2001) produces several classification trees, which are used to classify (Breiman et al., 2017). RF classifiers consist of multiple classifiers trained independently on bootstrapped training samples. Each tree in the random forest is constructed from a distinct subset of training samples. The trees predict the output class of testing samples independently, and the final decision is based on majority voting. The splitting of nodes is done based on a feature's Gini-

index, and the process continues until a stopping criterion is met. An essential requirement for ensembles of decision trees to be more effective than any one of its individual members, according to (Hansen and Salamon, 1990), is that the ensemble's members mitigate randomness and are heterogeneous. The diversity across classification trees is boosted by resampling the sample with substitution and randomly varying the predictive variable sets across the various tree induction procedures. Among the many advantages of the algorithm, there is no need to scale, convert, or otherwise alter the data from the RF method; it is able to resist outliers and takes care of the missing data automatically. The RF model has been successfully applied in bio-informatics (Qi, 2012), genetics, eco-hydrology (Li et al., 2020), ecology, and earth sciences (Confuorto et al., 2022), yielding generally accurate results. Several works confirm how the RF approaches are the most performing multi-class classifier algorithm (Breiman et al., 2017; Pal, 2005).
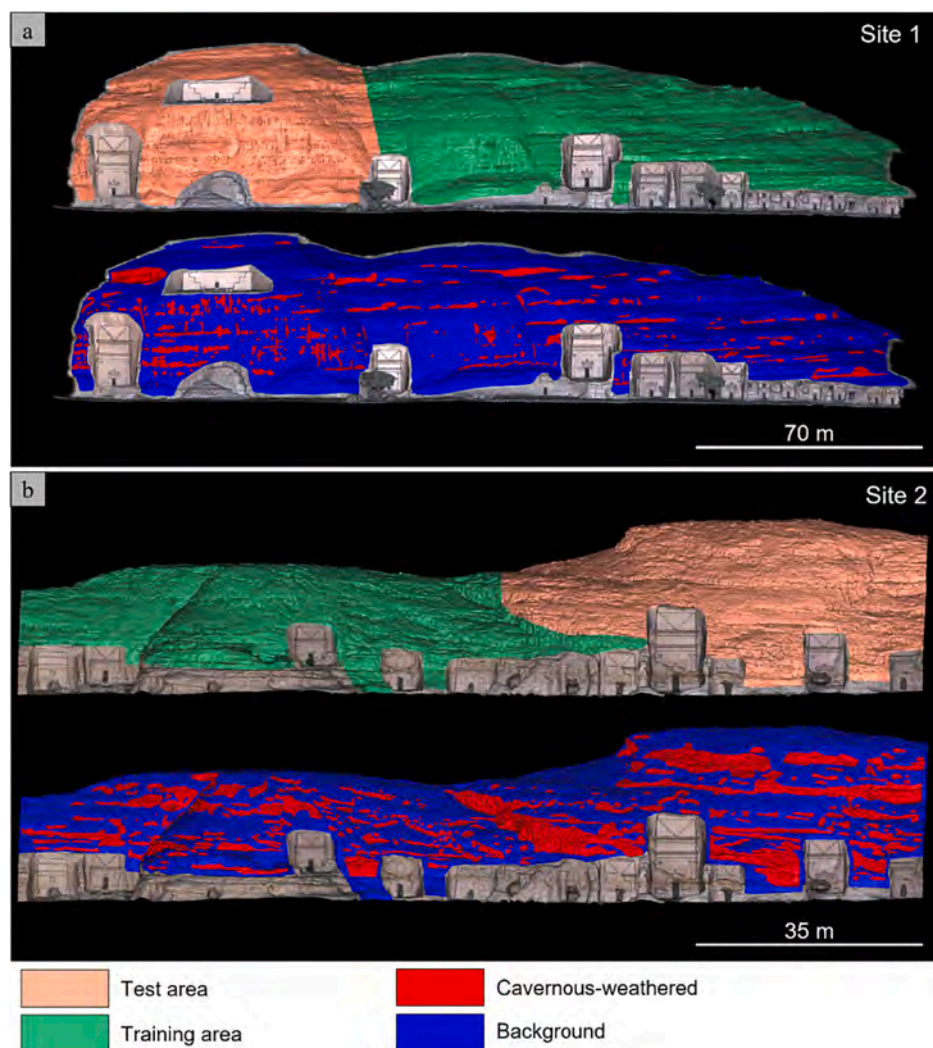
Fig. 9. Panoramic views of the two studied rock slopes. In a) the Necropolis of Jabal al-Khraymāt (Site 1) and b) the Necropolis of Qaṣr al-Bint. Both slopes have been used to calibrate and evaluate the RF model. Each site was divided into a training area (green) and a test area (light orange). Manual segmentation of cavernous-weathered areas (red) was carefully performed for each site. (For interpretation of the references to colour in this figure legend, the reader is referred to the web version of this article.)

3.4. Model calibration and evaluation

Two rock slopes (site 1 in Fig. 9a and site 2 in Fig. 9b) were used to train and evaluate the model performance. A random division of points into train and test sets would have heavily biased the model performance by increasing the final scores since adjacent points carry similar variable values. Therefore, we have decided to divide the point cloud sets geometrically using the manual segmentation tool of CC. So, we have created two training areas and two testing areas (Fig. 9).

The two training areas were used together as a unique training dataset and the other two as two different testing areas (see Fig. 9). In fact, to verify the generalization of the model it is recommended to train and test the model not in the same dataset but whenever possible in different testing areas (see Table A.1 for train only on site 1 and test only on site 2, and vice versa). For this model, the test and train datasets come from the same Archaeological area but from two different rock slopes (Fig. 2 and Fig. 9), this has been done to consider the heterogeneity of

the weathering process acting in Hegra depending on the lithologic features exposition. Manual segmentation was carried out to determine two classes: cavernous-weathered areas (CW) and background (back). All the categorization results were manually labelled to ensure their reliability. Expert-created labels are meant to be as near to "ground truth" as feasible (Fig. 9). As a result, in the proposed investigation, classification performance is assessed by comparing model predictions to the authors' hand labelling. However, despite the experience of the expert, the labelling process is subject to several biases in such extended and complex surfaces. So, it is recommended to discuss and validate the final results of the implemented RF model, i.e., the classification performance. The points of the two defined training areas (Fig. 9) were used together to train the model. Table 2 shows the number of points for the complete training set, and the two test sets defined. The ratio values CW/back shows a consistent imbalance between the two classes. We noticed that the high imbalance of the sets slightly influenced the modelling, therefore class weights were applied during training. We

Table 2
Number of points per class and ratio between classes for the training and test sets used in the research.

Dataset	Number of points			Ratio (CW/back)
	Cavernous Weathering (CW)	Background (back)	Total	
Complete training set	955,689	4,819,903	5,775,592	0.2
Site 1 test set	267,973	1,177,050	1,445,023	0.23
Site 2 test set	724,927	1,582,408	2,307,335	0.46

chose to have a difference in the class ratio of the test sets of sites 1 and 2 to evaluate the model performance in datasets with different ratio characteristics.

To evaluate the performance of the model, Accuracy (*a*) (Eq. 12), Precision (*p*), Recall (*r*), and F1-score (*f*) have been calculated using true positives (TP), true negatives (TN), false positives (FP), and false negatives (FN). Precision (Eq. 13; Lormand et al. (2018)) shows the proportion of points correctly detected by the model. Recall (Eq. 14) is the fraction of labelled data points correctly recognized by the model, and the F1-score (Eq. 15) represents the balance of the Precision and Recall metrics. Follow the definitions:

$$a = \frac{(TP + TN)}{(TP + TN + FP + FN)} \tag{12}$$

$$p = \frac{TP}{(TP + FP)} \tag{13}$$

$$r = \frac{TP}{(TP + FN)} \tag{14}$$

$$f = 2 \cdot \frac{p \cdot r}{(p + r)} \tag{15}$$

3.5. Kinematic analysis

To have as clear knowledge as possible on the potential instabilities processes active on the most endangered studied rock slope of Jabal al-Khraymāt (site 1), and to understand if there is a correlation between the CW and instability processes, a kinematic analysis was carried out using the DiAna-K MATLAB routine (Gigli and Casagli, 2011; Gigli et al., 2022). The latter represents an upgrade of the established DiAna routine approach (Gigli and Casagli, 2011) used to semi-automatically extract six of the ten key parameters suggested by the International Society for Rock Mechanics (Barton, 1978) to quantitatively describe rock-mass discontinuities: orientation, number of sets, spacing, persistence, block size, and JRC. DiAna operates via a searching cube, or voxel of space, which iteratively examines the studied point cloud. A best fitting plane is created using the points falling within the searching cube by applying user defined threshold values relative to the acceptable number of points falling inside the searching cube and the acceptable standard deviation of the best fitting plane. After the plane has been created, it is possible to determine the dip and dip/direction values as well as the other parameters (for a detailed explanation refer to Gigli and Casagli, 2011). Based on the extracted discontinuity properties, the DiAna-K routine allowed us to semi-automatically calculate the probability of structurally controlled instabilities based on kinematic tests; each mesh element orientation is evaluated against each extracted discontinuity plane and intersection values for both "normal" and "overhanging" rock slopes (for a detailed explanation refer to Gigli et al., 2022). The DiAna-K approach return the spatial distribution of the following instability mechanisms: free fall failure (FF), flexural toppling failure (FT), block toppling failure (BT), wedge failure (WF), and plane failure (PF). To achieve it, a susceptibility value (*S*) was calculated for each mechanism:

$$S_{FF} = 1 - \left(1 - \frac{N_{FF}}{N}\right) \cdot \left(1 - \frac{I_{FF}}{I}\right) \tag{16}$$

$$S_{WF} = \frac{I_{WF}}{I} \cdot 100 \tag{17}$$

$$S_{PF} = \frac{N_{PF}}{N} \cdot 100 \tag{18}$$

$$S_{FT} = \frac{N_{FT}}{N} \cdot 100 \tag{19}$$

$$S_{BT} = \frac{N_{BT}}{N} \cdot \frac{I_{BT}}{I} \cdot 100 \tag{20}$$

Where *N* is the total number of poles and *I* is the total number of intersections, while N_{FF}, N_{PF}, N_{FT}, N_{BT} and I_{FF}, I_{WF}, and I_{BT} are, respectively, the poles and the intersections falling into the critical areas of the stereographic plots obtained using the user-inputted data (discontinuity orientations and JRC) in the DiAna-K routine. A global kinematic index (*GKI*) was calculated by combining all the aforementioned rock failure mechanisms (Gigli et al., 2022) to obtain the overall rockfall susceptibility. *GKI* is defined as follows:

$$GKI = 1 - (1 - S_{PF} - N_{FF} - S_{FT}) \cdot (1 - S_{WF} - I_{FF}) \cdot (1 - S_{BT}) \tag{21}$$

The kinematic analysis highlights the rock slope areas more prone to the instability mechanisms. These insights were compared and integrated with the AI-inferred cavernous weathering inventory to obtain a preliminary assessment of the most endangered rock slope sectors.

4. Results

4.1. Automated cavernous weathering detection

The RF model was trained by using all the following geometric features: λ_1, λ_2, λ_3, Σ, *O*, *E*, *A*, *P*, *L*, *S*, PCA1, PCA2, *SV*, *V*. Each feature was calculated for 10 different kernel radiuses (0.2 m, 0.4 m, 0.6 m, 0.8 m, 1 m, 1.2 m, 1.4 m, 1.6 m, 1.8 m, 2 m), so a total of 160 variables were used by the model (see all the features created boxplot in Figs. A.1-A.8 in Appendix A). 100 model training runs (after shuffling the training set before each run) were performed to check the model stability when predicting on the unseen test sets. The variability values of the used metrics are shown in Table 3, along with the metrics scores. Feature selection criteria through variable importance and operator experience were separately applied to the dataset to attempt to reduce the number of variables and increase the model performance. However, in all cases, we noticed a decrease in the model performance. Therefore, for the final modelling, all the variables were used to train the RF model. Table 3 lists the scores of the RF model (*a, p, r, f*) carried out on the two test sets defined in this study.

We noticed that the high imbalance of the sets slightly influenced the modelling, although class weights were manually imbalanced while training. This is testified by the differences in the recalls between the weathering and background classes. However, the model was able to reliably predict the cavernous weathered areas, with a small tendency to

Table 3
Random Forest testing results on site 1, site 2, and site 1 + 2. In the columns, the values of Accuracy (*a*; Eq. 12), Precision (*p*; see Eq. 13), Recall (*r*; see Eq. 14), F1-score (*f*; see Eq. 15), and the number of points is reported.

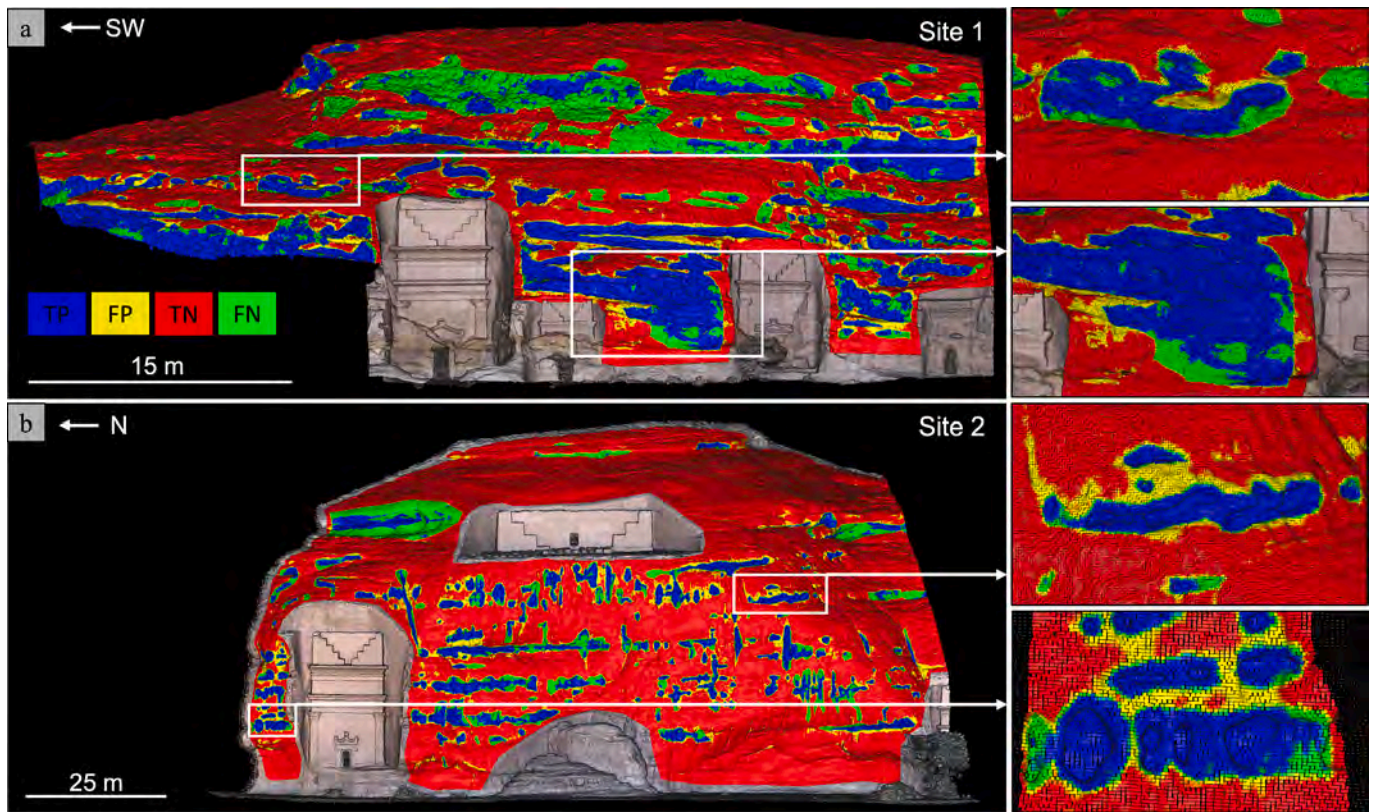| Site	Class	a (%)	p (%)	r (%)	f (%)	Sample points (#)
1 + 2	Background	86.61 ± 0.01	87.91 ± 0.02	94.84 ± 0.02	91.24 ± 0.01	2,759,449
	Weathering		81.64 ± 0.05	63.75 ± 0.06	71.59 ± 0.03	992,900
1	Background	89.17 ± 0.02	91.73 ± 0.02	95.29 ± 0.02	93.48 ± 0.01	1,177,041
	Weathering		75.05 ± 0.06	62.28 ± 0.09	68.07 ± 0.06	267,973
2	Background	85.02 ± 0.02	85.25 ± 0.02	94.51 ± 0.03	89.64 ± 0.01	1,582,408
	Weathering		84.29 ± 0.06	64.29 ± 0.06	72.95 ± 0.04	724,927

Fig. 10. Confusion matrix results visualized using colours on the point cloud of the studied rock slopes: true positives (TP), true negatives (TN), false positives (FP), and false negatives (FN). In a) sector II of the Necropolis of Jabal al-Khraymāt; in b) Necropolis of Qaṣr al-Bint. On the right, some zooms on the cavernous-weathered surfaces are reported.
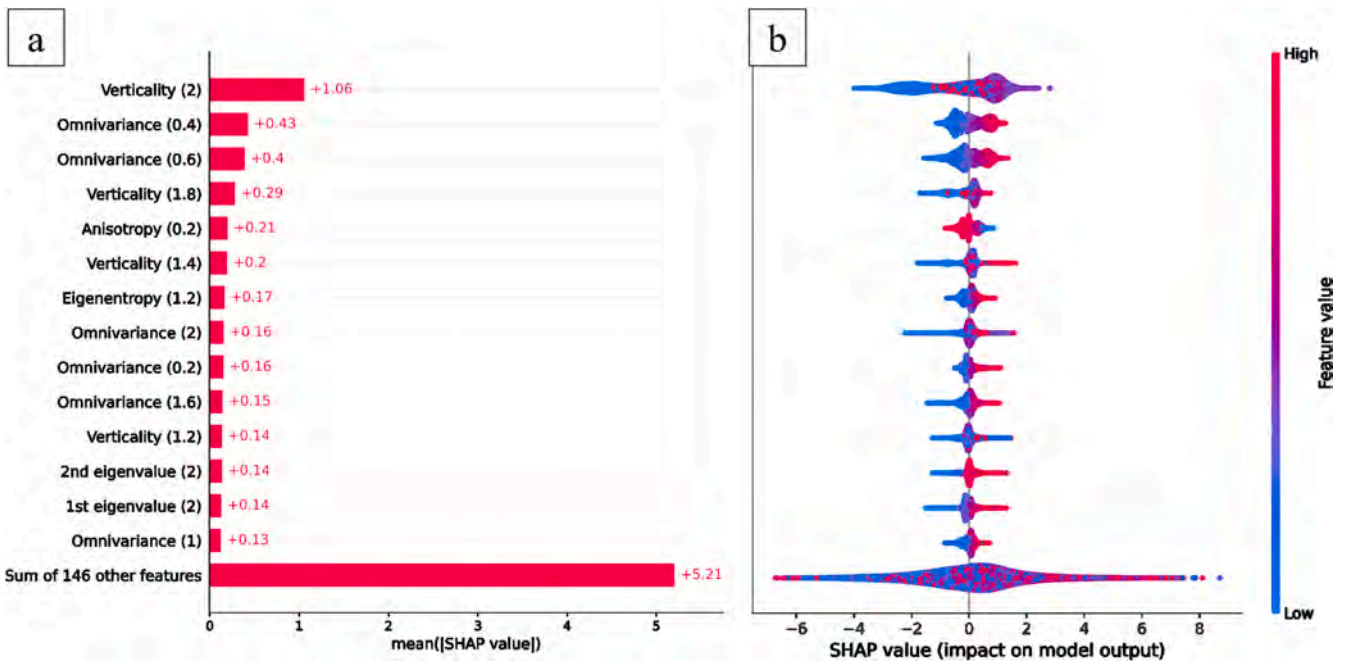

Fig. 11. SHAP plots (Van den Broeck et al., 2022) for the 15 most important variables (mixed test set): a) the mean absolute SHAP values, which represents the absolute impact of a certain variable on model prediction; b) beeswarm plot showing the positive and negative impacts of variable SHAP values on the model predictions, the colour shows the original variable value.

underpredict the same, as shown by the slightly low recall, while showing a small number of false positives, as shown by the high precision.

To provide meaningful visual insights of the predictions, the point cloud of the training area has been coloured with a scalar field representing the TP, FP, TN, and FN. This view allows us to rapidly understand how the model works. There are some sectors at the top of the slope of site 1 with a lot of FN (green points). This is due to the UAV-DP process to create the dense point cloud. The higher part of the slope was characterized by a lower number of survey photos, resulting in a less rough surface point cloud after the SfM processing. So, we have manually identified all these areas as CW even if the point cloud data tends to be "slightly less rough" and so "slightly less cavernous" to be recognized by the RF model. This phenomenon did not occur on the lower part of the slope, near the tombs, where more photos were taken during the UAV survey and the hollows (alveoli and *tafoni*) were reconstructed much more accurately in the point cloud and therefore more easily recognized as TP by the trained model.

On the right side of Fig. 10, some zoomed images of well-predicted areas on both site 1 and site 2 are shown. It is visible the accuracy of the model in the identification of *tafoni* and alveoli with dimensions ranging from 50 cm up to 3 m. The presence of FP points (yellow points) and FN (green points) along the edges of the TP points must be seen as a bias caused by the subjectivity of the manual labelling process, that sometimes led to label cavities individually and sometimes as an entire area, containing both the hollows that the space between them (rock walls and ribs).

4.2. Explainable AI (XAI) insights on model predictions

The trained model outputs have been investigated using an open-source XAI python library called SHAP (Van den Broeck et al., 2022). Fig. 11a shows the variable importance (in terms of mean SHAP values) as well as a more representative plot called beeswarm (Fig. 11b) for the most important 15 variables, from which it is possible to understand the influence of the variable value in relation to the model decision when predicting the mixed test set. Results highlight that the verticality calculated within a two-meter kernel radius, i.e., a searching sphere of 4 m diameter, is by far the most important variable. Verticality has a negative high contribution on low values (blue colour in Fig. 11b), while a positive low contribution on medium values (red colour). We can also see some high values of Verticality randomly distributed (for kernel
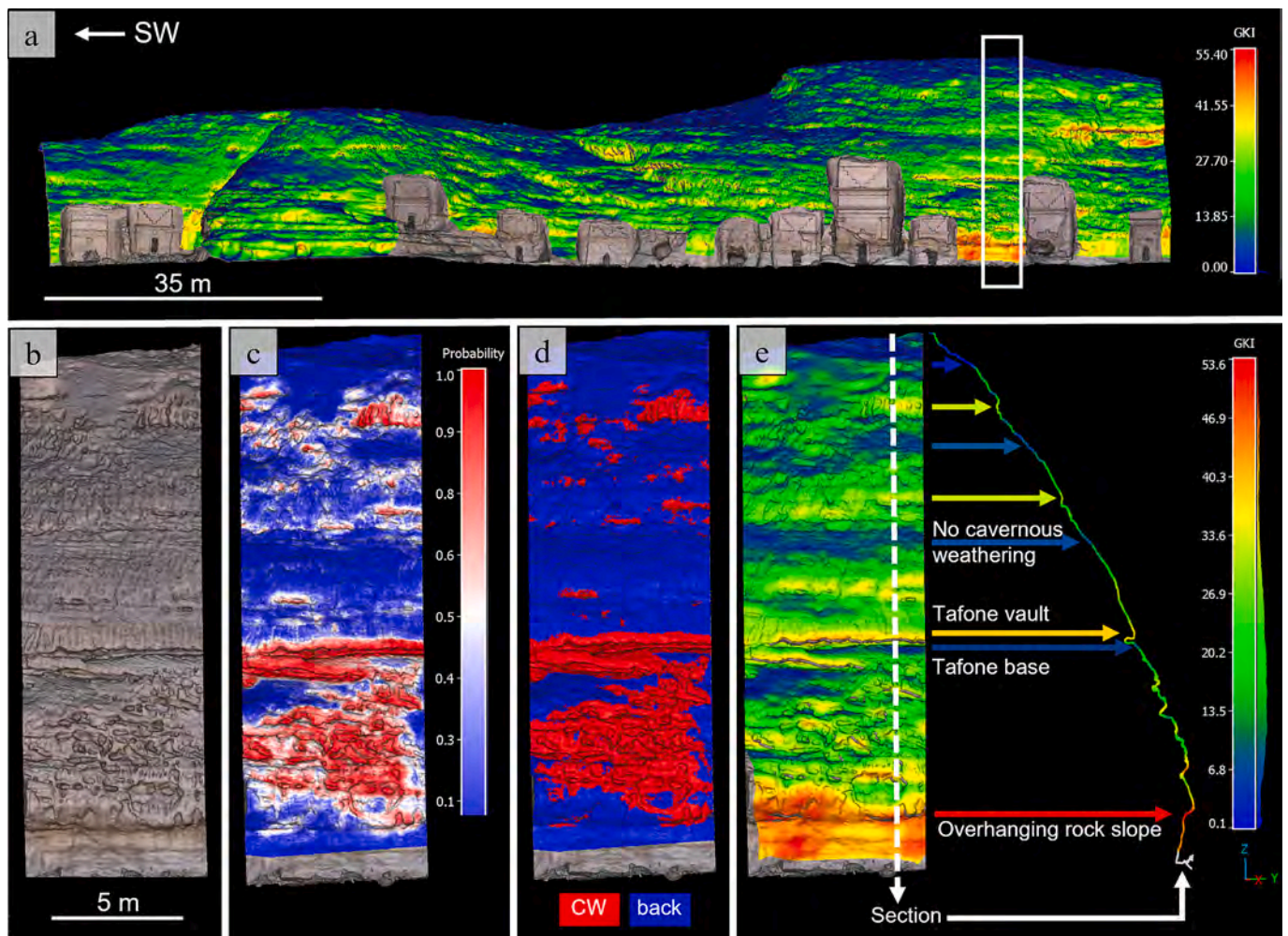

Fig. 12. Results of the three-dimensional kinematic analysis carried out using the DiAna-K algorithm and comparison with AI-aided classification. In a) the susceptibility values relative to the global kinematic index (GKI) are draped on the UAV-DP obtained rock slope mesh, the GKI reaches values up to 55%, the white polygon highlights an example sector of the slope; b) the RGB mesh of the chosen slice sector is shown; c) the probability values of AI-aided classification in cavernous-weathered areas (CW) and background areas (back), 1 mean CW areas and 0 back with a 0.5 threshold; d) displaying of CW and back areas relative to the probability shown in c); e) GKI values reached in the considered slice sector, along the white dotted line a section of the distribution of GKI values along the rock slope is shown.

radius of 1.2 m, 1.4 m, 1.8 m), which might be misleading for the model. The importance of verticality within this range of searching spheres can be interpreted in two ways: as the predisposition of the sub-vertical sectors of the rock slope, extended >2 m^2, to cavernous weathering; or conversely, that the cavernous weathering erosion processes have led some rock slope sectors to faster deterioration through the action of instability mechanisms (FF, PF, WF, BT, FT) and chemical deterioration of the sandstone, increasing the verticality of the rock slope, up to the overhanging.

The Omnivariance with 0.4 and 0.6 m radius occupy the second and third positions respectively. Omnivariance variables have a high positive contribution when their values are high, and a low negative contribution on low values (Fig. 11b). Anisotropy with a 0.2 m radius (a searching sphere of 0.4 m) is in fourth place, and it shows that high values have a negative contribution, while it has a positive contribution on low values. Instead, Eigenentropy is found at the seventh position, with a positive contribution on high values. More generally, except for Omnivariance and Anisotropy, the 15 most important variables are those calculated using kernel radius higher than 1 m, i.e., searching spheres of at least 2 m diameter.

4.3. Global kinematic index (GKI)

To obtain a reliable assessment of the potential instabilities processes active on the most endangered studied rock slope (sector II of Jabal al-Khraymāt, site 1) and to understand the overall rockfall susceptibility of the slope, the DiAna-K MATLAB routine was successfully applied to highlight the areas more prone to instability processes. A global kinematic index (GKI) was calculated by combining the susceptibility values of the other structurally controlled instability mechanisms (FF, PF, WF, BT and FT) by applying Eq. Eq. 21. The comparison between the GKI values distribution and the cavernous weather surface areas (CW) allows to confirm the coincidence between the CW together with the higher GKI values. Therefore, the AI-aided assessment of alveoli and *tafoni* features not only allowed the identification of the most weathered area but also the areas most prone to instability processes. The spatial distribution of the RF model classification and GKI values within the weathered rock slope area are shown in Fig. 12. The availability of the RGB mesh of the slope (example slice in Fig. 12b) allowed us to understand the intensity of the erosional phenomena acting on the rock slope surfaces and to directly compare the accuracy of the RF model in detecting the most weathered ones. In addition, higher values of GKI (red colour in Fig. 12a-
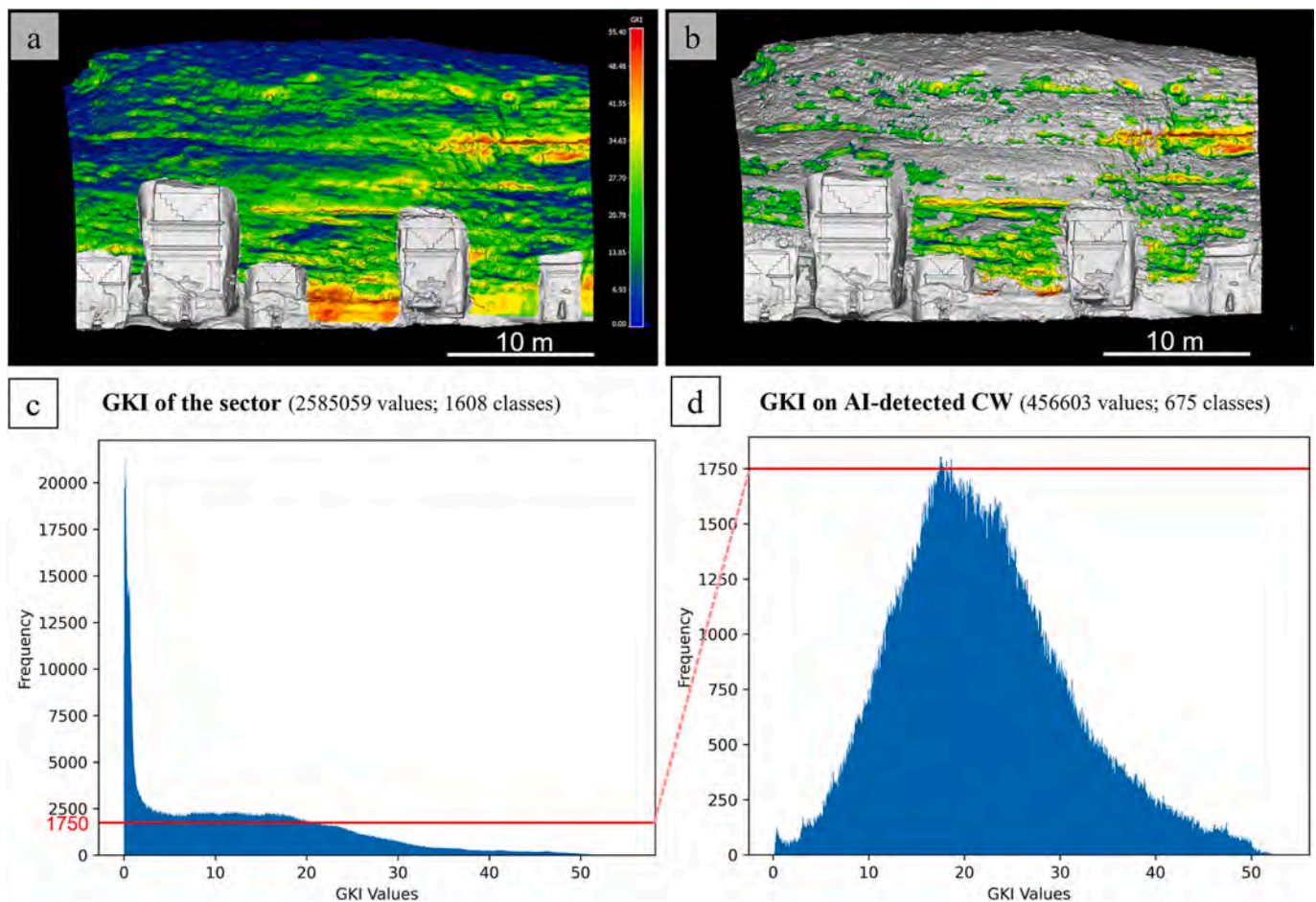

Fig. 13. Comparative analysis and visualization of the cavernous-weathered areas (CW) identified using AI-based approaches related to the global kinematic index (GKI) derived from kinematic analysis. In a) the overall GKI values on the chosen sector, providing an overview of the susceptibility values on the slope, and b) the GKI values relative to the AI-detected CW areas. In c) and d) the distribution of the GKI values from a) and b), respectively. The correlation between the presence of CW and the occurrence of higher GKI values is readily discernible, particularly on the non-overhanging sections of the rock slope where cavernous weathering processes are actively developing.

e) occur in the overhanging slope sectors where more instability mechanisms are feasible at the same time (highest value of FF) but, considering the entire slope, the majority of the non-overhanging sectors with high GKI values coincide with the most cavernous-weathered areas, that caused predisposing factors to failure (see Fig. 4c-d-e-g).

In Fig. 13a, the GKI values are shown for the testing sector of site 1, and in Fig. 13b, only the GKI values relative to the point of the cavernous-weathered areas identified by the RF model are shown. The distribution of the GKI values in Fig. 13c-d confirms the fact that, on average, the GKI reaches higher values in weathered areas. Therefore, for similar lithologies and settings, the kinematic analysis should consider the weathering state of the slope. Furthermore, if no data about discontinuity sets, JRC, or JCS are available, i.e., no kinematic analysis could be performed, the detection of cavernous-weathered areas using only the proposed RF model could provide preliminary insights on the most unstable areas.

5. Discussion

In this paper, an AI-aided method to detect cavernous-weathered areas on rock slopes using geometric features calculated on three-dimensional data is presented. To this aim, several synthetic and real rock slopes were analysed to understand how the geometric features work to detect cavernous weathering, i.e., *tafoni*, alveoli, and honeycombs. Nowadays, the management and classification processes of the three-dimensional dataset created using TLS and/or UAV-DP methods are becoming a topic of growing interest worldwide (Becker et al., 2018; Brodu and Lague, 2012; Lague et al., 2013; Lichti, 2005; Pal, 2005; Weidner et al., 2019; Weinmann et al., 2013, 2017). Several proposed classification methods suggest how to discriminate 3D vegetation features from 2D surfaces (Brodu and Lague, 2012; Carlberg et al., 2009), or manufactures, roofs, and streets in an urban environment (Weinmann et al., 2013, 2017). The proposed method aims to detect complex geomorphological erosional features overwhelming the difficulties linked to the manual monitoring process.

5.1. RF model for weathering assessment

The employment of the AI method together with geometric features calculation to classify the three-dimensional point cloud weathered areas represent integration and enrichment of the knowledge about the topic of automated classification methods. The latter has become a fundamental research topic for three-dimensional data management. Nowadays, projects with billions of points are becoming more and more frequent in everyday surveys. Automatic segmentation of large three-dimensional point clouds could be improved and calibrated for each case to reduce the time-consuming manual labelling of the operator involved in such analysis as much as possible (and reduce subjectivity). This methodology starts from a raw point cloud that needs to be cleaned and oriented ad hoc for the training and testing of the RF model. All the variables utilized by the model are calculated from geometric features extracted from the point cloud, so, errors in the point cloud might negatively influence the accuracy of the model.

In this study, two UAV-DP-derived point clouds were used. We show that the UAV-DP dataset works well in slope sectors where the SfM algorithm creates an accurate point cloud (more tie points) of the hollows. In fact, in the upper part of the slope, where a few photos were taken, the SfM algorithm was not able to correctly reconstruct all the inner parts (back and vault) of the hollows. The smallest alveoli appear as black holes in the UAV-taken photos; therefore, it was not possible to reconstruct the inner shape of such cavities. Furthermore, the "ground truth" we have manually designed (in the training and test areas of the two slopes) tended to "over-classify" the weathered area, considering also little honeycombs that the RF model did not predict as cavities (the FN in Fig. 10).

The amount of training data was sufficient to calibrate a reliable

classifier in terms of number of points (millions of points per rock wall). However, we believe that the number of hollows present in a single rock slope is not sufficient to calibrate a model and generalize it for all existing alveoli and *tafoni* sizes and shapes present in the entire area (see Table 1). Nevertheless, as visible from the results, this approach can yield reliable predictions when trained and tested in adjacent areas of the rock slope. The use of geometric features might allow the approach to be easily transferred and applied on other point clouds generated by different instruments and methods (TLS, ALS and UAV-DP). Moreover, as explained above, the point surrounding information is fed to the model through pre-selected 3D geometric features. It would be interesting to test deep learning models able to autonomously consider 3D relationships, such as PointCNN (Li et al., 2018) for such a task. However, to train such models, a huge amount of training instances is needed (and not easily accessible).

From the feature importance analysis, we noticed that no PCA variables appeared in the first 15 variables in the RF model, and we pointed out that this is one of the reasons why the CANUPO tool is slightly less accurate for this kind of purpose. In fact, (Brodu and Lague, 2012) chose "to compute PCA in the searching sphere as it is a simple and standard tool for finding relevant directions in the neighbourhood ball".

In ML model optimization, feature selection is a method of reducing features to increase model performance and reduce computing time. The goal of this strategy is to discover the ideal collection of features that will offer the greatest fit for the model and lead to increased prediction accuracy. Micheletti et al. (2014) emphasized the significance of feature selection and discussed the use of machine learning (ML) models such as a support vector machine (SVM), random forest (RF), and AdaBoost (Adaptive Boosting). In our research, instead, reducing the number of features results in poorer predictions with respect to when using all the 160 original features. This behaviour contradicts what is usually experienced by ML users, where feature selection usually plays an important role in boosting model performance (and/or maintaining similar performance while reducing computational time) (Meena et al., 2022). This means that each radius for each feature has a positive contribution to the final model predictions.

5.2. Cavernous weathering and instability processes assessment

The AI-aided classification of point clouds is a challenging topic because every scenario has different boundary conditions; the accuracy of the available survey data and the available machine-time to carry out the analysis. Despite there are significant differences in terms of point density and accuracy between the TLS and UAV-DP methods, these techniques are often used together when an aerial laser scanner (ALS) survey is not available.

The results pointed out the importance of detecting the weathered area on these sandstone rock slopes of Hegra. Here, instability processes such as FF, PF, WF, BT, and FT are mainly caused by the overhanging sector i.e., the high values of GKI at the overhanging foot of the slope (Fig. 13a), and the action of cavernous weathering (there are no dominant joint sets) that leads to detachment and rock fall. Therefore, the mapping of the spatial distribution of weathering highlights the potential rock fall source areas and the dimensions of the block depend on the dimensions of the hollows (see Fig. 4c-d); the larger the cavity, the larger is the potential volume of the falling blocks. The latter are represented by the vault of the hollows or by the ribs and thin rock wall between the alveoli.

6. Conclusion

From 2020 to 2022, several close-range and field survey campaigns were conducted at the World Heritage Site of Hegra, in AlUla (Kingdom of Saudi Arabia) with the primary aim of assessing the potential geohazards affecting the property. Using the UAV-DP-created point cloud we have trained and tested an RF model to rapidly classify the rock

slopes affected by cavernous weathering. The latter is the main cause of future potential instability processes acting on the outcropping sandstone of Hegra (Fig. 4). The results of the kinematic analysis carried out at the studied rock slopes confirmed the correlation between the presence of cavernous weathering and higher GKI susceptibility values. This is particularly true for the non-overhanging sections of the rock slopes (Figs. 12 and 13). To verify the reliability of the proposed AI-aided method, it was applied in the sector II of the Necropolis of Jabal al-Khraymāt (site 1) and the Necropolis of Qaṣr al-Bint (site 2).

The achieved results are the following:

● The RF model demonstrated a high level of precision in predicting areas of significant weathering on the studied rock slopes, with an accuracy rate of up to 85% (Table 3). It had a slight tendency to underestimate these regions, as evident from the relatively lower recall value (~ 63%) and minimal number of false positive predictions (Fig. 10), as reflected in the high accuracy rate. This approach can be easily reproduced without requiring significant computational resources, human labor, or financial investment. The utilization of the SHAP value in relation to the variable employed in the model enables the acquisition of both quantitative and spatial comprehension concerning the distribution of cavernous weathering phenomena and its intensity on the slope;
● Spatial correlation was observed between the calculated GKI values, which assess the overall rock fall susceptibility of the slope, and the identified cavernous weathering areas. The utilization of the RF model provided valuable insights into locations with elevated susceptibility values resulting from weathering-related instabilities. Particularly, areas with higher GKI values, reaching up to 55%, are closely aligned with the most weathered regions. Consequently, the successful implementation of this RF model represents a notable advancement in geo-hazard assessment at the Archaeological Site of Hegra.

Future challenges:

● Evaluation of the proposed approach on other weathered rock slopes of different lithologies and geological settings;
● Improvement of generalization capabilities of the RF model for a larger amount of three-dimensional point cloud data;
● The application of the model to the whole archaeological area of Hegra, also using a TLS survey when it will be available, to reduce the numbers of FN and FP caused by the difficulty of UAV-DP to reconstruct the inner part of the hollows;
● Evaluation of advanced deep learning models to automatically detect cavernous-weathered areas.

These findings offer valuable insights for various further analyses, encompassing the identification of run-out source areas, conducting simulations, designing mitigation strategies, and planning maintenance efforts. These plans also include the planning and design of touristic paths at the bottom of the slope, taking into consideration rockfall hazards associated with the cavernous weathering. The implications of this study extend well beyond Hegra, representing a significant step forward in comprehending and addressing potential geo-hazards in other similar rock-carved cultural heritage sites. The presented method establishes a solid foundation for future advancements in this specialized field of study, opening up possibilities for additional research and applications in the broader context of preserving and managing risk at rock-carved cultural heritage sites.

CRediT authorship contribution statement

Tommaso Beni: Visualization, Methodology, Investigation, Data curation, Conceptualization, Software, Writing - original draft, Writing - review & editing. **Lorenzo Nava:** Software, Methodology, Formal analysis, Conceptualization, Writing - original draft, Writing - review & editing. **Giovanni Gigli:** Supervision, Software, Validation, Writing - review & editing. **William Frodella:** Supervision, Investigation, Writing - review & editing. **Filippo Catani:** Supervision, Writing - review & editing. **Nicola Casagli:** Supervision, Funding acquisition, Writing - review & editing. **José Ignacio Gallego:** Supervision, Project administration, Funding acquisition, Writing - review & editing. **Claudio Margottini:** Supervision, Project administration, Investigation, Funding acquisition, Writing - review & editing. **Daniele Spizzichino:** Supervision, Investigation, Funding acquisition, Project administration, Writing - review & editing.

Declaration of Competing Interest

The authors declare that they have no known competing financial interests or personal relationships that could have appeared to influence the work reported in this paper.

Data availability

Data will be made available on request.
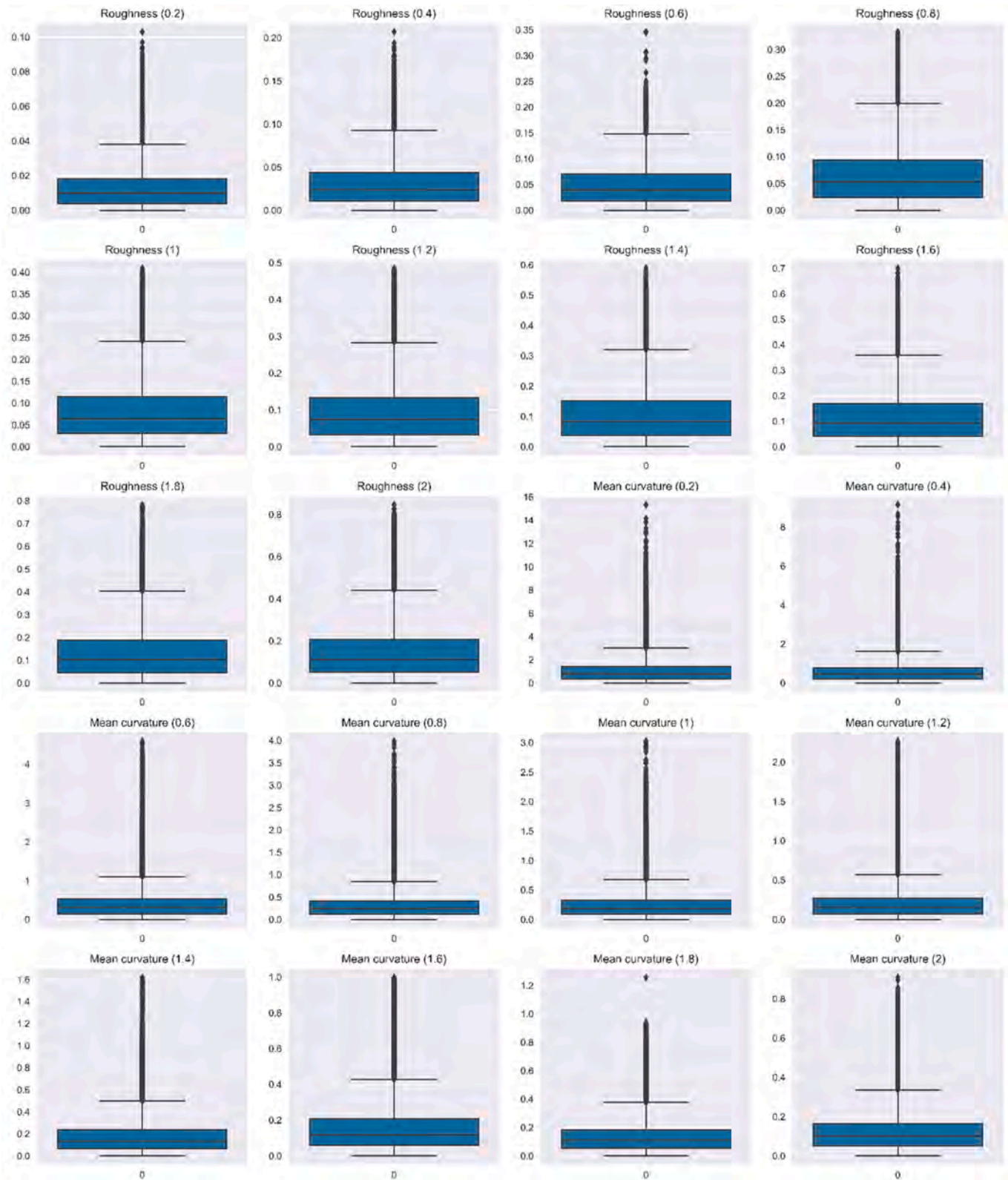
Appendix A

Fig. A.1. Geometric features values for 10 kernel radius: Roughness and Mean curvature.
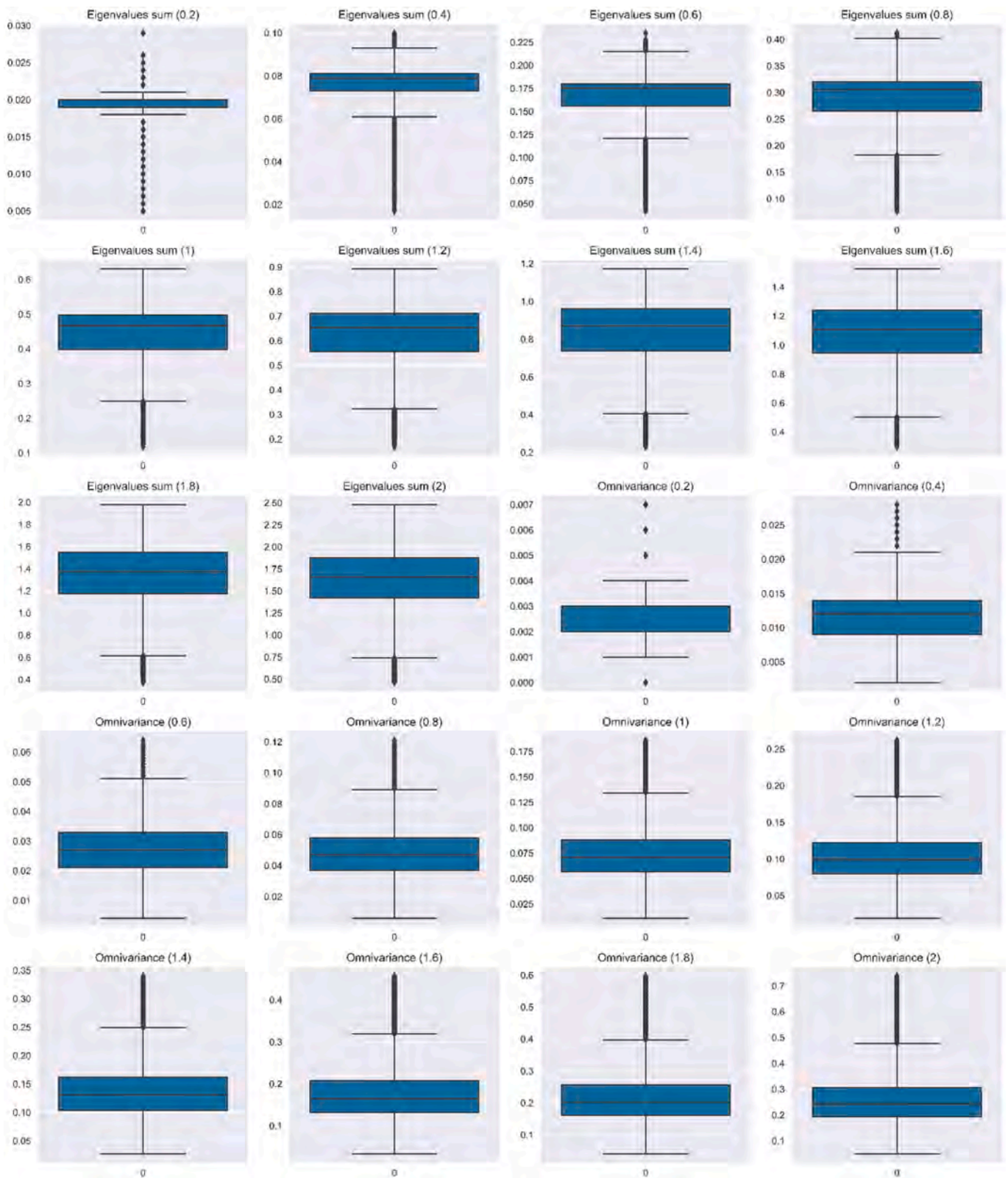
Fig. A.2. Geometric features values for 10 kernel radius: Eigenvalues sum and Omnivariance.
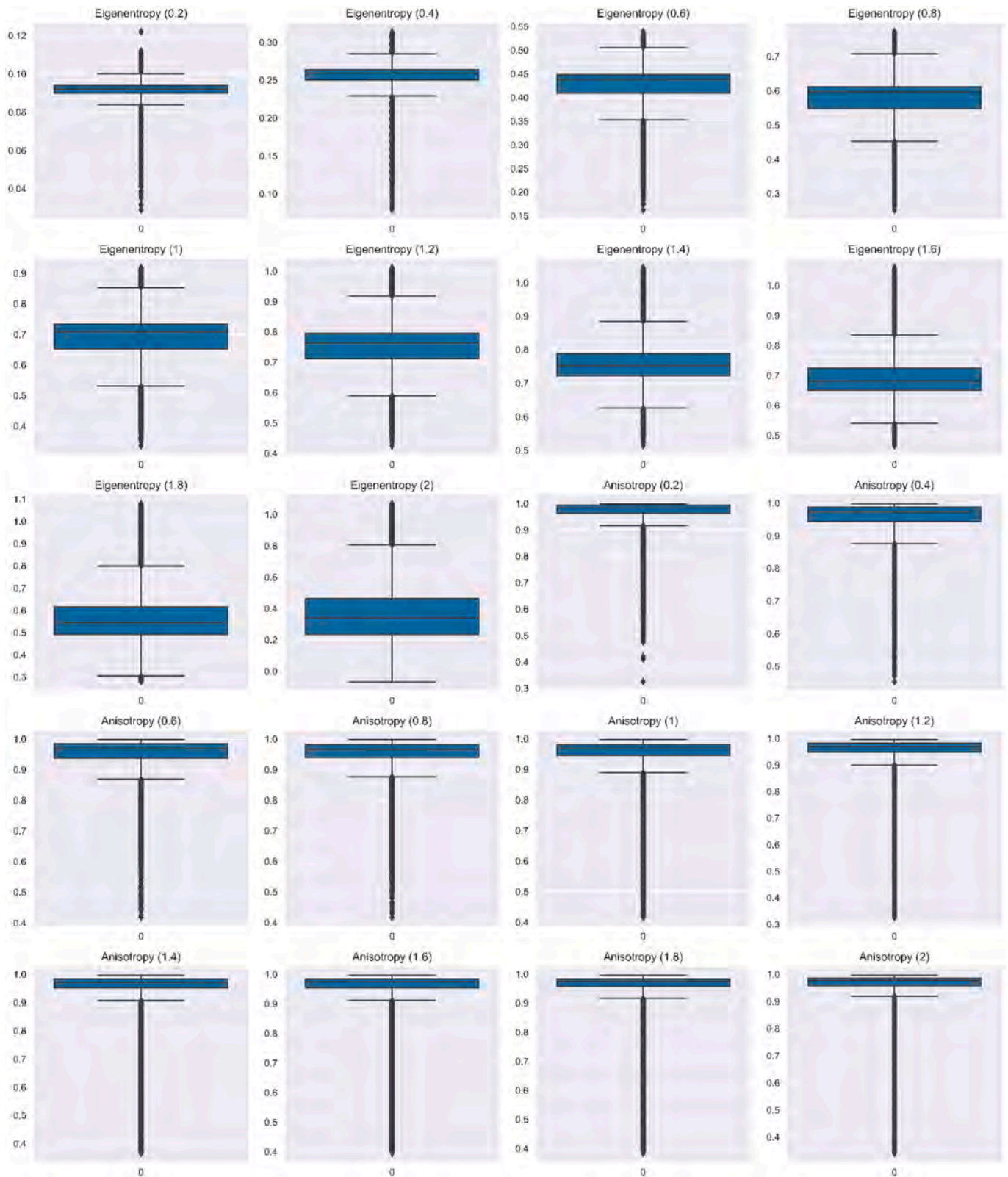
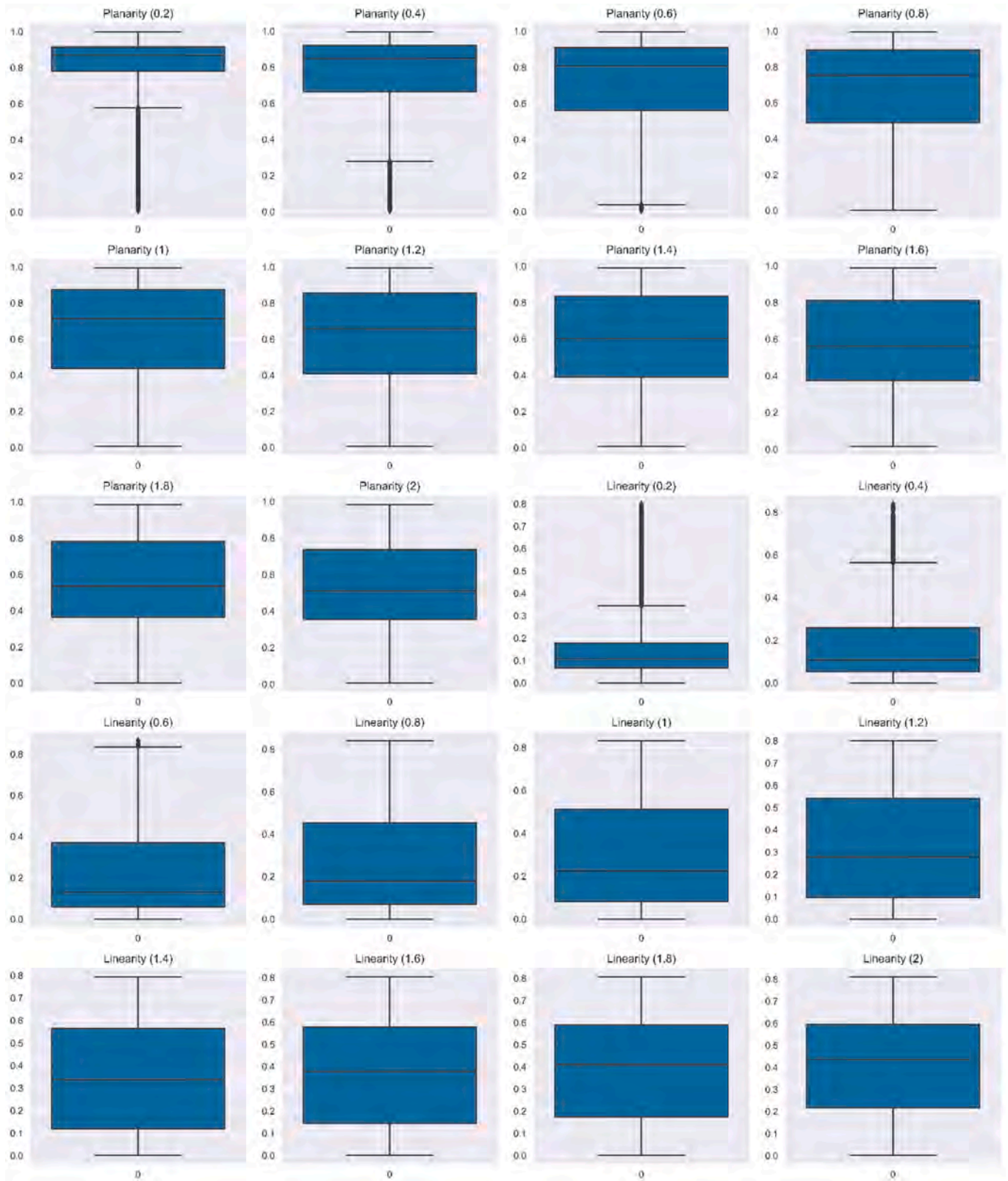**Fig. A3.** Geometric features values for 10 kernel radius: Eigenentropy and Anisotropy.

Fig. A.4. Geometric features values for 10 kernel radius: Planarity and Linearity.
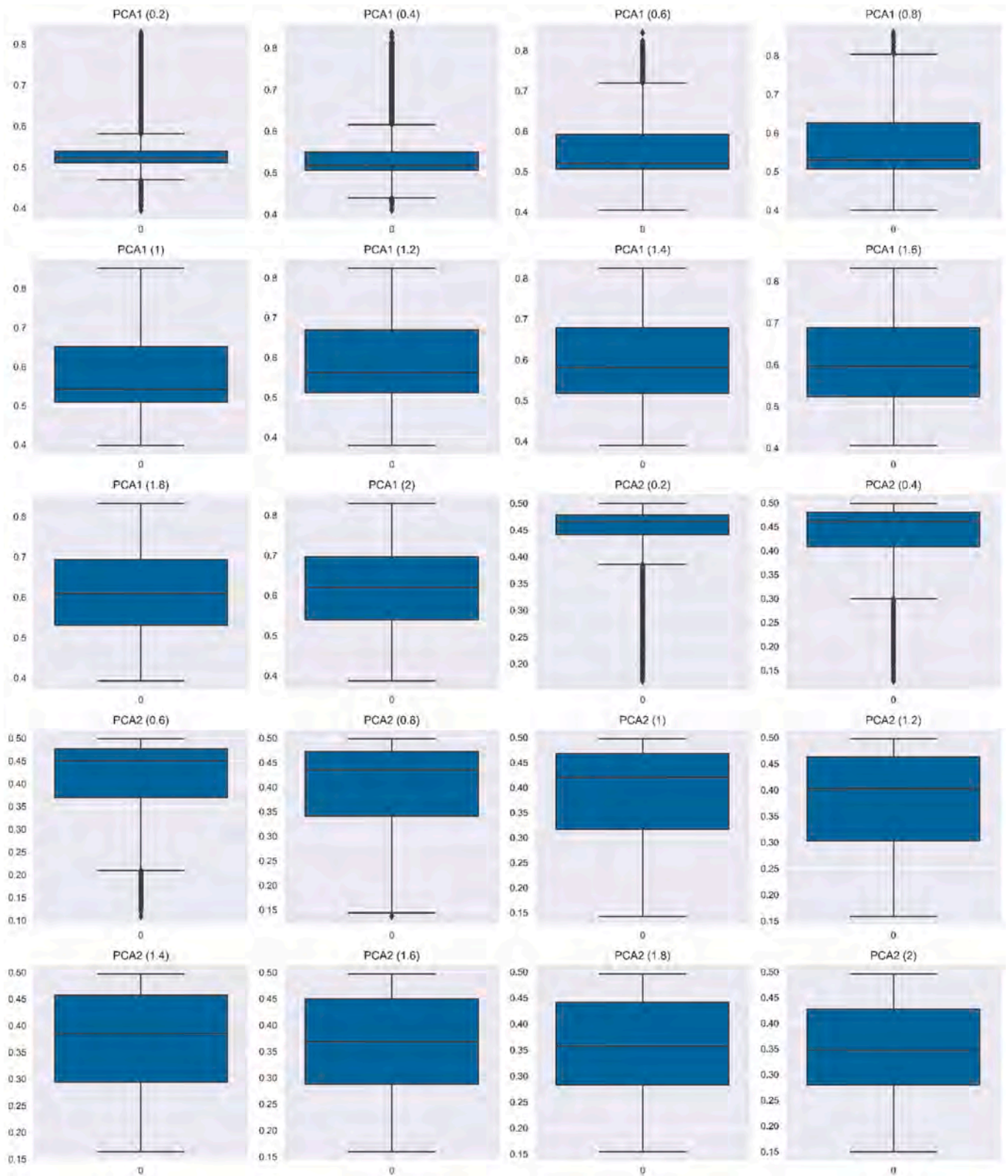
Fig. A.5. Geometric features values for 10 kernel radius: PCA1 and PCA2.
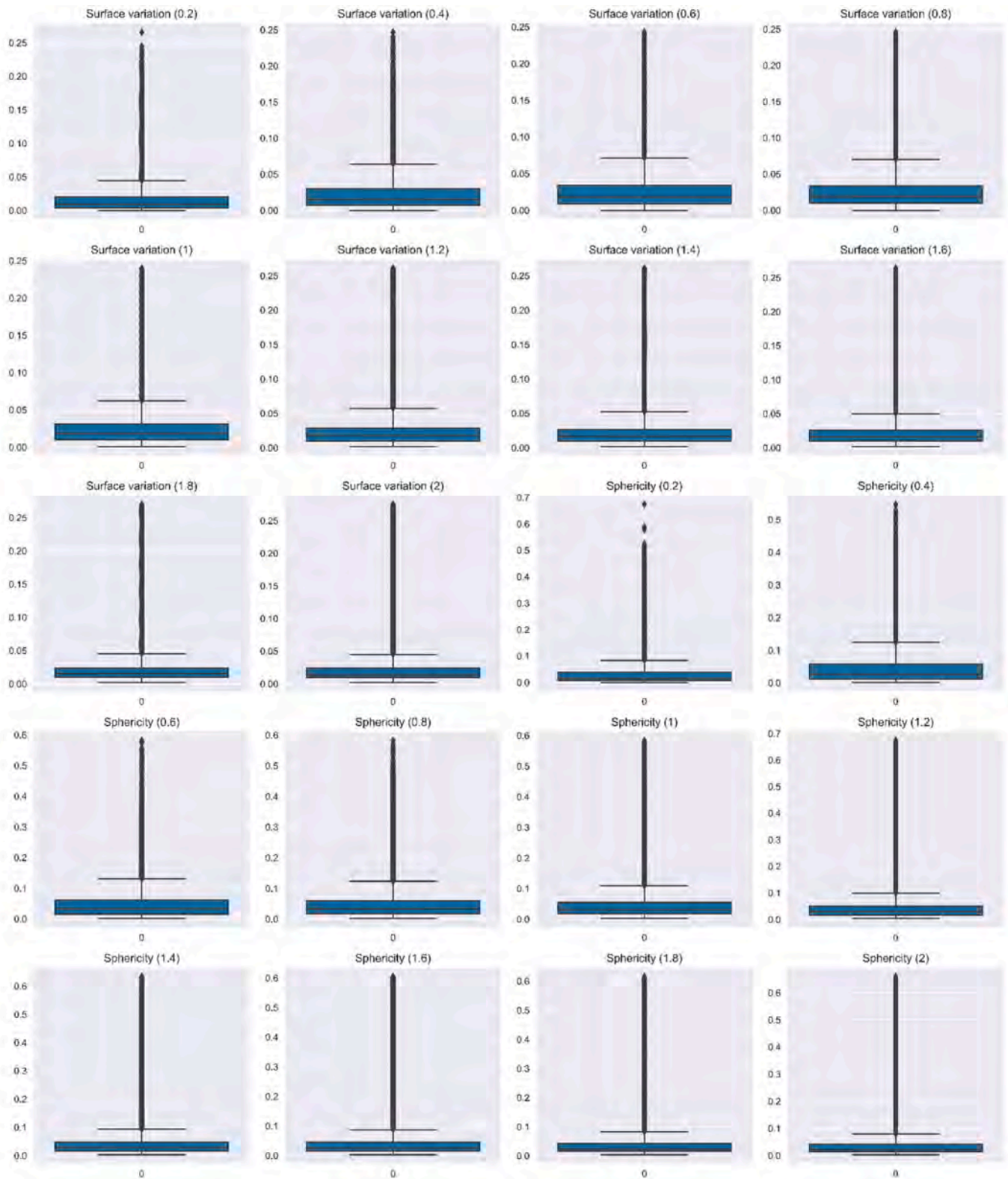
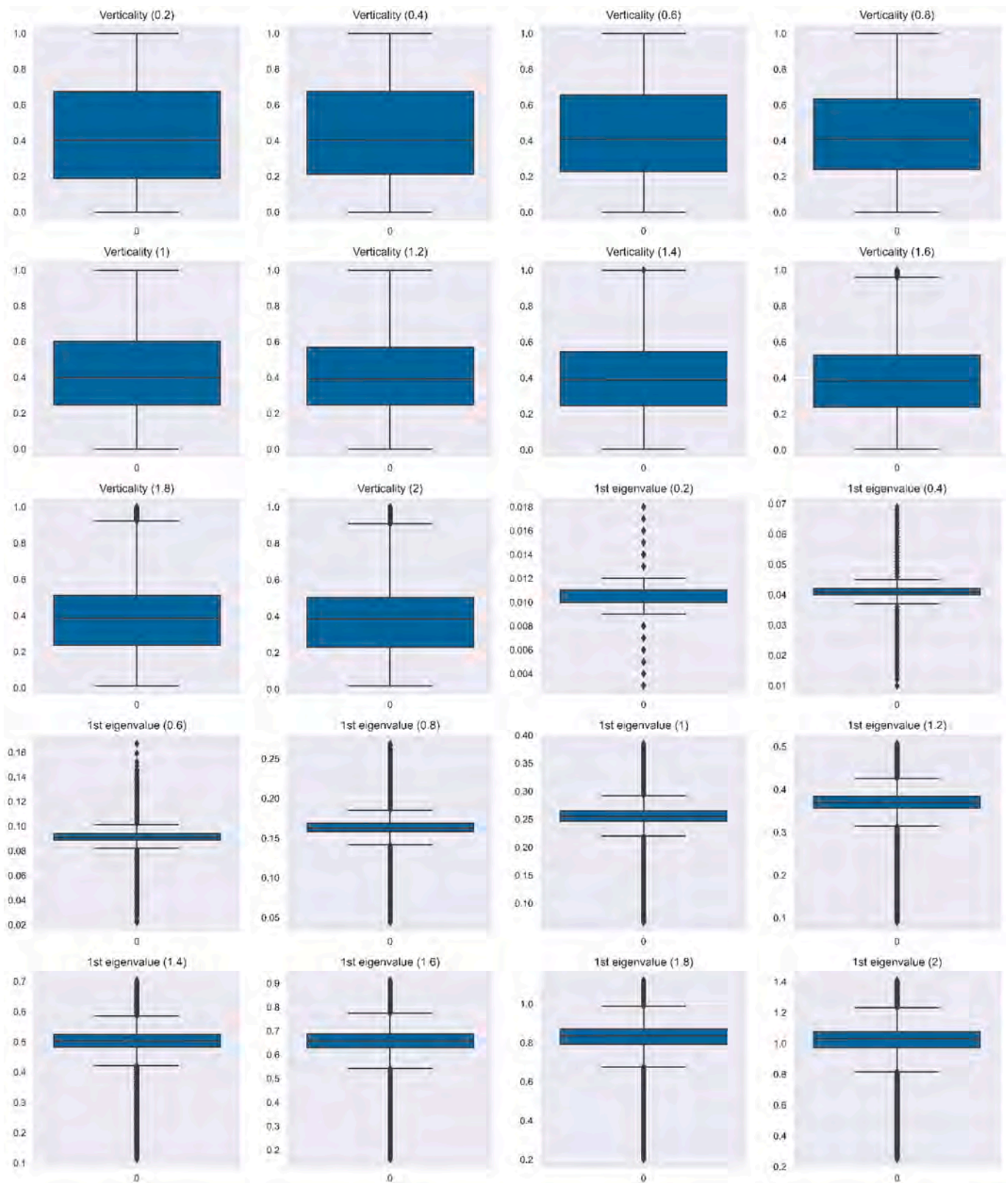**Fig. A.6.** Geometric features values for 10 kernel radius: Surface variation and Sphericity.

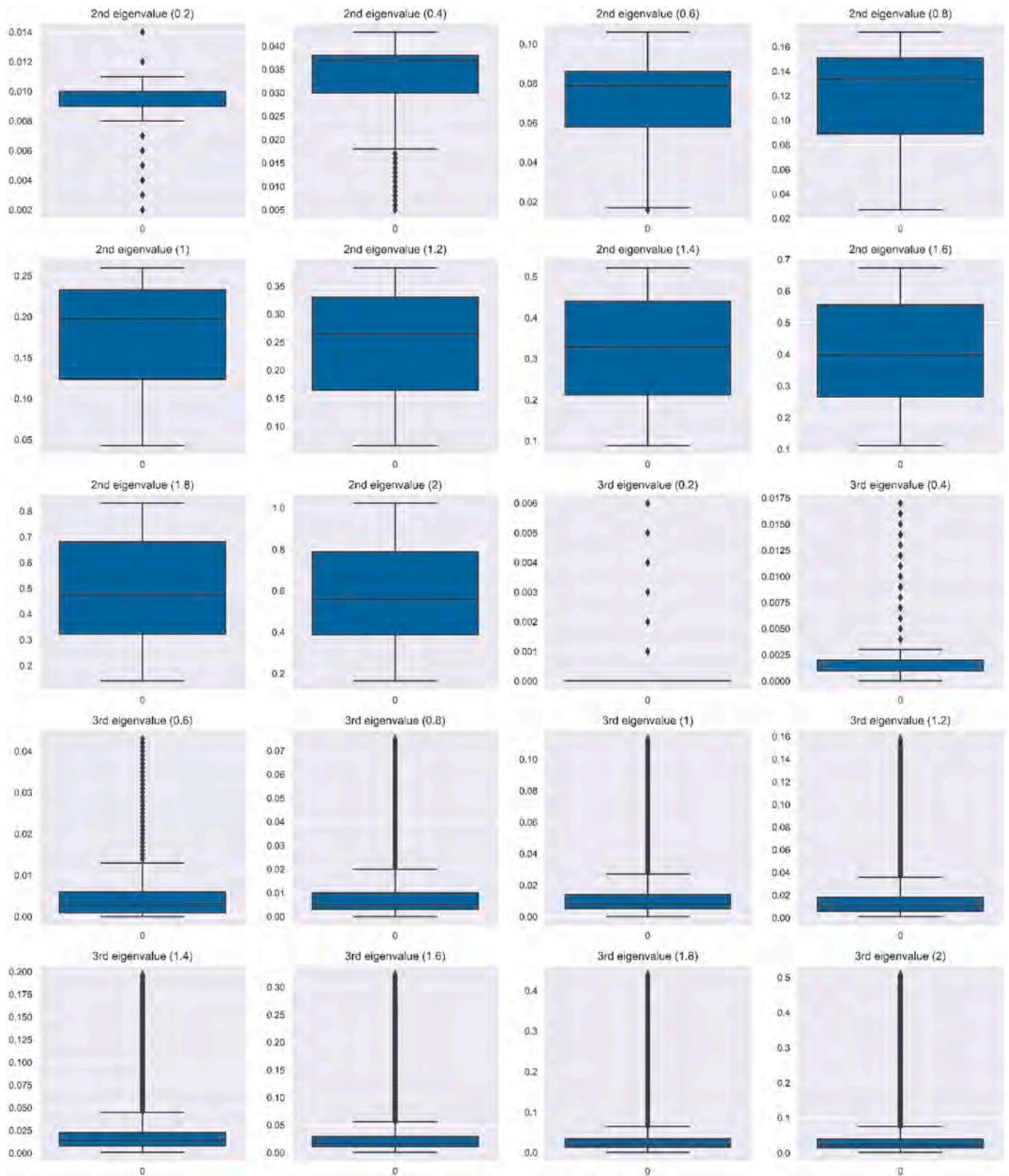**Fig. A.7.** Geometric features values for 10 kernel radius: Verticality and 1st eigenvalue.

Fig. A.8. Geometric features values for 10 kernel radius: 2nd eigenvalue and 3rd eigenvalue.

Table A.1

Random Forest cross testing results on site 1, site 2. In the first case, (1 to 2), the model is trained on the training set of site 1 and tested in the test set of site 2, while in the second case (2 to 1), the model is trained of the training set of site 2, and tested in the test set of site 1. In the columns, the values of Accuracy (a; Eq. 12), Precision (p; see Eq. 13), Recall (r; see Eq. 14), F1-score (f; see Eq. 15), and the number of points is reported.

Site	Class	a (%)	p (%)	r (%)	f (%)	Sample points (#)
1 to 2	Background	74	94	72	82	1,177,041
	Weathering		40	53	53	267,973
2 to 1	Background	83	82	96	88	1,582,408
	Weathering		87	53	66	724,927

References

Abellán, A., Jaboyedoff, M., Oppikofer, T., Vilaplana, J.M., 2009. Detection of millimetric deformation using a terrestrial laser scanner: experiment and application to a rockfall event. Nat. Hazards Earth Syst. Sci. 9, 365–372. https://doi.org/10.5194/nhess-9-365-2009.

Balek, J., Blahůt, J., 2017. A critical evaluation of the use of an inexpensive camera mounted on a recreational unmanned aerial vehicle as a tool for landslide research. Landslides 14, 1217–1224. https://doi.org/10.1007/s10346-016-0782-7.

Barton, N., 1978. Suggested methods for the quantitative description of discontinuities in rock masses. ISRM Int. J. Rock Mech. Min. Sci. Geomech. Abstr. 15, 319–368.

Battulwar, R., Zare-Naghadehi, M., Emami, E., Sattarvand, J., 2021. A state-of-the-art review of automated extraction of rock mass discontinuity characteristics using three-dimensional surface models. J. Rock Mech. Geotech. Eng. 13, 920–936. https://doi.org/10.1016/j.jrmge.2021.01.008.

Becker, C., Rosinskaya, E., Häni, N., D'Angelo, E., Strecha, C., 2018. Classification of Aerial Photogrammetric 3D Point Clouds. Photogramm. Eng. Remote. Sens. 84, 287–295. https://doi.org/10.14358/PERS.84.5.287.

Beni, T., Gigli, G., Lombardi, L., Carlà, T., Casagli, N., 2022. Route stability index (RSI): an index for the assessment of rockfall-related hazards in rock slopes equipped for sport climbing. Geoheritage 14, 80. https://doi.org/10.1007/s12371-022-00715-7.

Blanco, L., García-Sellés, D., Guinau, M., Zoumpekas, T., Puig, A., Salamó, M., Gratacós, O., Muñoz, J.A., Janeras, M., Pedraza, O., 2022. Machine learning-based rockfalls detection with 3D point clouds, example in the Montserrat Massif (Spain). Remote Sens. 14, 4306. https://doi.org/10.3390/rs14174306.

Blomley, R., Weinmann, M., Leitloff, J., Jutzi, B., 2014. Shape distribution features for point cloud analysis – a geometric histogram approach on multiple scales. ISPRS Ann. Photogramm. Remote Sens. Spat. Inf. Sci. II 3, 9–16. https://doi.org/10.5194/isprsannals-II-3-9-2014.

Boldini, D., Guido, G.L., Margottini, C., Spizzichino, D., 2018. Stability analysis of a large-volume block in the historical rock-cut city of Vardzia (Georgia). Rock Mech. Rock. Eng. 51, 341–349. https://doi.org/10.1007/s00603-017-1299-7.

Bouchaud, C., Sachet, I., Dal Prà, P., Delhopital, N., Douaud, R., Leguilloux, M., 2015. New discoveries in a Nabataean tomb. Burial practices and 'plant jewellery' in ancient Hegra (Madâ'in Sâlih, Saudi Arabia). Arab. Archaeol. Epigr. 26, 28–42. https://doi.org/10.1111/aae.12047.

Breiman, L., 2001. Random forest. Mach. Learn. 45, 5–32. https://doi.org/10.1023/A:1010933404324.

Breiman, L., Friedman, J.H., Olshen, R.A., Stone, C.J., 2017. Classification and Regression Trees, 1st ed. Routledge. https://doi.org/10.1201/9781315139470.

BRGM [WWW Document], 2022. GIS Data Bur. Rech. Geol. Min. Saudi Geol. Surv. SGS. URL. https://tiles.arcgis.com/tiles/r1KRjdBe86hriMWS/arcgis/rest/services/GeologyMaps_BRGM250_Mosaic/MapServer?cacheKey=b50355f57d1d9f71.

Brodu, N., Lague, D., 2012. 3D terrestrial lidar data classification of complex natural scenes using a multi-scale dimensionality criterion: applications in geomorphology. ISPRS J. Photogramm. Remote Sens. 68, 121–134. https://doi.org/10.1016/j.isprsjprs.2012.01.006.

Bruthans, J., Filippi, M., Slavík, M., Svobodová, E., 2018. Origin of honeycombs: testing the hydraulic and case hardening hypotheses. Geomorphology 303, 68–83. https://doi.org/10.1016/j.geomorph.2017.11.013.

Carlberg, M., Gao, P., Chen, G., Zakhor, A., 2009. Classifying urban landscape in aerial LiDAR using 3D shape analysis, in: 2009 16th IEEE International Conference on Image Processing (ICIP). In: Presented at the 2009 16th IEEE International Conference on Image Processing ICIP 2009, IEEE, Cairo, Egypt, pp. 1701–1704. https://doi.org/10.1109/ICIP.2009.5413385.

CloudCompare, 2022. CloudCompare [WWW Document]. URL. https://www.danielgm.net/cc/ (accessed 4.27.22).

Confuorto, P., Medici, C., Bianchini, S., Del Soldato, M., Rosi, A., Segoni, S., Casagli, N., 2022. Machine learning for defining the probability of Sentinel-1 based deformation trend changes occurrence. Remote Sens. 14, 1748. https://doi.org/10.3390/rs14071748.

DiFrancesco, P.-M., Bonneau, D., Hutchinson, D.J., 2020. The implications of M3C2 projection diameter on 3D semi-automated rockfall extraction from sequential terrestrial laser scanning point clouds. Remote Sens. 12, 1885. https://doi.org/10.3390/rs12111885.

Donald, G., Hadly, G., 1987. Explanatory Notes to the Geological Map of the Sahl Al Matran Quadrangle 1–24.

Frodella, W., Elashvili, M., Spizzichino, D., Gigli, G., Adikashvili, L., Vacheishvili, N., Kirkitadze, G., Nadaraia, A., Margottini, C., Casagli, N., 2020. Combining InfraRed thermography and UAV digital photogrammetry for the protection and conservation of rupestrian cultural heritage sites in Georgia: a methodological application. Remote Sens. 12, 892. https://doi.org/10.3390/rs12050892.

Froideval, L., Pedoja, K., Garestier, F., Moulon, P., Conessa, C., Pellerin Le Bas, X., Traoré, K., Benoit, L., 2019. A low-cost open-source workflow to generate georeferenced 3D SfM photogrammetric models of rocky outcrops. Photogramm. Rec. 34, 365–384. https://doi.org/10.1111/phor.12297.

Gallego, J.I., Margottini, C., Spizzichino, D., Boldini, D., Abul, J.K., 2022. Geomorphological processes and rock slope instabilities affecting the AlUla archaeological region. In: Geotechnical Engineering for the Preservation of Monuments and Historic Sites III. CRC Press, London, pp. 456–466. https://doi.org/10.1201/9781003308867-31.

Gigli, G., Casagli, N., 2011. Semi-automatic extraction of rock mass structural data from high resolution LIDAR point clouds. Int. J. Rock Mech. Min. Sci. 48, 187–198. https://doi.org/10.1016/j.ijrmms.2010.11.009.

Gigli, G., Lombardi, L., Carlà, T., Beni, T., Casagli, N., 2022. A method for full three-dimensional kinematic analysis of steep rock walls based on high-resolution point cloud data. Int. J. Rock Mech. Min. Sci. 157, 105178. https://doi.org/10.1016/j.ijrmms.2022.105178.

Groom, K.M., Allen, C.D., Mol, L., Paradise, T.R., Hall, K., 2015. Defining tafoni: Re-examining terminological ambiguity for cavernous rock decay phenomena. Prog. Phys. Geogr. Earth Environ. 39, 775–793. https://doi.org/10.1177/0309133315605037.

Hackel, T., Wegner, J.D., Schindler, K., 2016. Contour detection in unstructured 3D point clouds. In: 2016 IEEE Conference on Computer Vision and Pattern Recognition (CVPR). Presented at the 2016 IEEE Conference on Computer Vision and Pattern Recognition (CVPR). IEEE, Las Vegas, NV, USA, pp. 1610–1618. https://doi.org/10.1109/CVPR.2016.178.

Hansen, L.K., Salamon, P., 1990. Neural network ensembles. IEEE Trans. Pattern Anal. Mach. Intell. 12, 993–1001. https://doi.org/10.1109/34.58871.

Har'el, Z., 1995. Curvature of Curves and Surfaces—A Parabolic Approach. Department of Mathematics.

Heinrichs, K., 2008. Diagnosis of weathering damage on rock-cut monuments in Petra, Jordan. Environ. Geol. 56, 643–675. https://doi.org/10.1007/s00254-008-1358-1.

Jennings, J.N., 1968. Tafoni. Geomorphology, Encyclopedia of Earth Science. Kluwer Academic Publishers, Dordrecht, pp. 1103–1104. https://doi.org/10.1007/3-540-31060-6_365.

Klimchouk, A., 2018. Tafoni and honeycomb structures as indicators of ascending fluid flow and hypogene karstification. Geol. Soc. Lond. Spec. Publ. 466, 79–105. https://doi.org/10.1144/SP466.11.

Kromer, R., Lato, M., Hutchinson, D.J., Gauthier, D., Edwards, T., 2017. Managing rockfall risk through baseline monitoring of precursors using a terrestrial laser scanner. Can. Geotech. J. 54, 953–967. https://doi.org/10.1139/cgj-2016-0178.

Lague, D., Brodu, N., Leroux, J., 2013. Accurate 3D comparison of complex topography with terrestrial laser scanner: Application to the Rangitikei canyon (N-Z). ISPRS J. Photogramm. Remote Sens. 82, 10–26. https://doi.org/10.1016/j.isprsjprs.2013.04.009.

Li, Y., Bu, R., Sun, M., Wu, W., Di, X., Chen, B., 2018. PointCNN: convolution on X-transformed points. In: Bengio, S., Wallach, H., Larochelle, H., Grauman, K., Cesa-Bianchi, N., Garnett, R. (Eds.), Advances in Neural Information Processing Systems. Curran Associates, Inc.

Li, M., Zhang, Y., Wallace, J., Campbell, E., 2020. Estimating annual runoff in response to forest change: a statistical method based on random forest. J. Hydrol. 589, 125168. https://doi.org/10.1016/j.jhydrol.2020.125168.

Lichti, D.D., 2005. Spectral filtering and classification of terrestrial laser scanner point clouds. Photogramm. Rec. 20, 218–240. https://doi.org/10.1111/j.1477-9730.2005.00321.x.

Lin, C.-H., Chen, J.-Y., Su, P.-L., Chen, C.-H., 2014. Eigen-feature analysis of weighted covariance matrices for LiDAR point cloud classification. ISPRS J. Photogramm. Remote Sens. 94, 70–79. https://doi.org/10.1016/j.isprsjprs.2014.04.016.

Liu, Q., Wronski, L., Danzl, P., 2021. Processing outcrop point clouds to 3D rock structure using open source software. IOP Conf. Ser. Earth Environ. Sci. 833, 012054 https://doi.org/10.1088/1755-1315/833/1/012054.

Lormand, C., Zellmer, G.F., Németh, K., Kilgour, G., Mead, S., Palmer, A.S., Sakamoto, N., Yurimoto, H., Moebis, A., 2018. Weka trainable segmentation plugin in ImageJ: a semi-automatic tool applied to crystal size distributions of microlites in volcanic rocks. Microsc. Microanal. 24, 667–675. https://doi.org/10.1017/S1431927618015428.

Mao, Z., Hu, S., Wang, N., Long, Y., 2021. Precision evaluation and fusion of topographic data based on UAVs and TLS surveys of a loess landslide. Front. Earth Sci. 9, 801293. https://doi.org/10.3389/feart.2021.801293.

Margottini, C., Gigli, G., Ruther, H., Spizzichino, D., 2016. Advances in sustainable conservation practices in rupestrian settlements inscribed in the UNESCO's world heritage list. Procedia Earth Planet. Sci. 16, 52–60. https://doi.org/10.1016/j.proeps.2016.10.006.

Meena, S.R., Soares, L.P., Grohmann, C.H., van Westen, C., Bhuyan, K., Singh, R.P., Floris, M., Catani, F., 2022. Landslide detection in the Himalayas using machine learning algorithms and U-Net. Landslides 19, 1209–1229. https://doi.org/10.1007/s10346-022-01861-3.

Menegoni, N., Giordan, D., Perotti, C., Tannant, D.D., 2019. Detection and geometric characterization of rock mass discontinuities using a 3D high-resolution digital outcrop model generated from RPAS imagery – Ormea rock slope, Italy. Eng. Geol. 252, 145–163. https://doi.org/10.1016/j.enggeo.2019.02.028.

Micheletti, N., Foresti, L., Robert, S., Leuenberger, M., Pedrazzini, A., Jaboyedoff, M., Kanevski, M., 2014. Machine learning feature selection methods for landslide susceptibility mapping. Math. Geosci. 46, 33–57. https://doi.org/10.1007/s11004-013-9511-0.

Nava, L., Monserrat, O., Catani, F., 2022. Improving Landslide Detection on SAR data through deep learning. IEEE Geosci. Remote Sens. Lett. 19, 1–5. https://doi.org/10.1109/LGRS.2021.3127073.

Nehmé, L., Bessac, J.-C., Braun, J.-P., Dentzer-Feydy, J. (Eds.), 2015. Les tombeaux nabatéens de Hégra, Épigraphie & archéologie. Académie des inscriptions et belles-lettres, Paris.

Pal, M., 2005. Random forest classifier for remote sensing classification. Int. J. Remote Sens. 26, 217–222. https://doi.org/10.1080/01431160412331269698.

Paradise, T.R., 2005. Petra revisited: an examination of sandstone weathering research in Petra, Jordan. In: Stone Decay in the Architectural Environment. Geological Society of America.. https://doi.org/10.1130/0-8137-2390-6.39.

Paradise, T.R., 2013. Assessment of tafoni distribution and environmental factors on a sandstone djinn block above Petra, Jordan. Appl. Geogr. 42, 176–185. https://doi.org/10.1016/j.apgeog.2013.04.011.

Pellicani, R., Argentiero, I., Manzari, P., Spilotro, G., Marzo, C., Ermini, R., Apollonio, C., 2019. UAV and airborne LiDAR data for interpreting kinematic evolution of landslide movements: the case study of the Montescaglioso landslide (Southern Italy). Geosciences 9, 248. https://doi.org/10.3390/geosciences9060248.

Pirotti, F., Tonion, F., 2019. Classification of aerial laser scanning point clouds using machine learning: a comparison between random forest and tensorflow. Int. Arch. Photogramm. Remote Sens. Spat. Inf. Sci. XLII 2/W13, 1105–1111. https://doi.org/10.5194/isprs-archives-XLII-2-W13-1105-2019.

Pix4D, 2022. Pix4Dmapper Software [WWW Document]. URL. https://www.pix4d.com/product/pix4dmapper-photogrammetry-software.

Qi, Y., 2012. Random Forest for Bioinformatics. In: Zhang, C., Ma, Y. (Eds.), Ensemble Machine Learning. Springer US, Boston, MA, pp. 307–323. https://doi.org/10.1007/978-1-4419-9326-7_11.

Robinson, D.A., Williams, R.B.G., 1994. Rock Weathering and Landform Evolution, British Geomorphological Research Group Symposia Series. J. Wiley & Sons, Chichester New York Brisbane [etc.].

Rodriguez-Navarro, C., Doehne, E., Sebastian, E., 1999. Origins of honeycomb weathering: the role of salts and wind. Geol. Soc. Am. Bull. 111, 1250–1255. https://doi.org/10.1130/0016-7606(1999)111<1250:OOHWTR>2.3.CO;2.

Sampietro-Vattuone, M.M., Peña-Monné, J.L., 2021. Application of 2D/3D models and alteration mapping for detecting deterioration processes in rock art heritage (Cerro Colorado, Argentina): a methodological proposal. J. Cult. Herit. 51, 157–165. https://doi.org/10.1016/j.culher.2021.08.006.

Sartre, M., 2016. Laïla Nehmé, Les tombeaux nabatéens de Hégra (Épigraphie et archéologie 2). Syria. https://doi.org/10.4000/syria.4415.

Seo, H., 2021. 3D roughness measurement of failure surface in CFA pile samples using three-dimensional laser scanning. Appl. Sci. 11, 2713. https://doi.org/10.3390/app11062713.

Son, S.W., Kim, D.W., Sung, W.G., Yu, J.J., 2020. Integrating UAV and TLS approaches for environmental management: a case study of a waste stockpile area. Remote Sens. 12, 1615. https://doi.org/10.3390/rs12101615.

Sturzenegger, M., Stead, D., 2009. Close-range terrestrial digital photogrammetry and terrestrial laser scanning for discontinuity characterization on rock cuts. Eng. Geol. 106, 163–182. https://doi.org/10.1016/j.enggeo.2009.03.004.

UNESCO [WWW Document], 2022. URL. https://whc.unesco.org/en/list/1293 (accessed 9.5.22).

Van den Broeck, G., Lykov, A., Schleich, M., Suciu, D., 2022. On the tractability of SHAP explanations. J. Artif. Intell. Res. 74, 851–886. https://doi.org/10.1613/jair.1.13283.

Vision, 2022. Vision 2030 [WWW Document]. Vis. 2030. URL. https://www.vision2030.gov.sa (accessed 9.15.22).

Weidner, L., Walton, G., Kromer, R., 2019. Classification methods for point clouds in rock slope monitoring: a novel machine learning approach and comparative analysis. Eng. Geol. 263, 105326. https://doi.org/10.1016/j.enggeo.2019.105326.

Weidner, L., Walton, G., Krajnovich, A., 2021. Classifying rock slope materials in photogrammetric point clouds using robust color and geometric features. ISPRS J. Photogramm. Remote Sens. 176, 15–29. https://doi.org/10.1016/j.isprsjprs.2021.04.001.

Weinmann, M., Jutzi, B., Mallet, C., 2013. Feature relevance assessment for the semantic interpretation of 3D point cloud data. ISPRS Ann. Photogramm. Remote Sens. Spat. Inf. Sci. II 5/W2, 313–318. https://doi.org/10.5194/isprsannals-II-5-W2-313-2013.

Weinmann, M., Jutzi, B., Mallet, C., Weinmann, M., 2017. Geometric features and their relevance for 3D point cloud classification. ISPRS Ann. Photogramm. Remote Sens. Spat. Inf. Sci. IV-1/W1, 157–164. https://doi.org/10.5194/isprs-annals-IV-1-W1-157-2017.

Whabi, A.M., 2014. Sedimentological and Stratigraphic Studies of the Cambro-Ordovician Succession in Northwest Saudi Arabia. (Master thesis). King Fahd University of Petroleum & Minerals, Dhahran – 31261, Saudi Arabia, Dhahran, Saudi Arabia.

Xie, Y., Tian, J., Zhu, X.X., 2020. Linking points with labels in 3D: a review of point cloud semantic segmentation. IEEE Geosci. Remote Sens. Mag. 8, 38–59. https://doi.org/10.1109/MGRS.2019.2937630.

Zoumpekas, T., Puig, A., Salamó, M., García-Sellés, D., Blanco Nuñez, L., Guinau, M., 2021. An intelligent framework for end-to-end rockfall detection. Int. J. Intell. Syst. 36, 6471–6502. https://doi.org/10.1002/int.22557.